The Astrophysical Journal, 754:114 (22pp), 2012 August 1 doi:10.1088/0004-637X/754/2/114

THE STRUCTURE AND EMISSION MODEL OF THE RELATIVISTIC JET IN THE QUASAR 3C 279 INFERRED FROM RADIO TO HIGH-ENERGY γ-RAY OBSERVATIONS IN 2008–2010

M. Hayashida[1,2], G. M. Madejski[1], K. Nalewajko[3,4], M. Sikora[4], A. E. Wehrle[5], P. Ogle[6], W. Collmar[7], S. Larsson[8,9,10], Y. Fukazawa[11], R. Itoh[11], J. Chiang[1], Ł. Stawarz[12,13], R. D. Blandford[1], J. L. Richards[14], W. Max-Moerbeck[14], A. Readhead[14], R. Buehler[1], E. Cavazzuti[15], S. Ciprini[15,16], N. Gehrels[17], A. Reimer[1,18], A. Szostek[1,13], T. Tanaka[1], G. Tosti[16,19], Y. Uchiyama[1], K. S. Kawabata[20], M. Kino[21], K. Sakimoto[11], M. Sasada[11], S. Sato[21], M. Uemura[20], M. Yamanaka[11], J. Greiner[7], T. Kruehler[22], A. Rossi[23], J. P. Macquart[24], D. C.-J. Bock[25], M. Villata[26], C. M. Raiteri[26], I. Agudo[27,28], H. D. Aller[29], M. F. Aller[29], A. A. Arkharov[30], U. Bach[31], E. Benítez[32], A. Berdyugin[33], D. A. Blinov[34], K. Blumenthal[28], M. Böttcher[35], C. S. Buemi[36], D. Carosati[37,38], W. P. Chen[39], A. Di Paola[40], M. Dolci[41], N. V. Efimova[30,34], E. Forné[42], J. L. Gómez[27], M. A. Gurwell[43], J. Heidt[44], D. Hiriart[45], B. Jordan[46], S. G. Jorstad[28,34], M. Joshi[28], G. Kimeridze[47], T. S. Konstantinova[34], E. N. Kopatskaya[34], E. Koptelova[39,48], O. M. Kurtanidze[47], A. Lähteenmäki[49], A. Lamerato[35], V. M. Larionov[30,34,50], E. G. Larionova[34], L. V. Larionova[34], P. Leto[36], E. Lindfors[33], A. P. Marscher[28], I. M. McHardy[51], S. N. Molina[27], D. A. Morozova[34], M. G. Nikolashvili[47], K. Nilsson[52], R. Reinthal[33], P. Roustazadeh[35], T. Sakamoto[17], L. A. Sigua[47], A. Sillanpää[33], L. Takalo[33], J. Tammi[49], B. Taylor[28,53], M. Tornikoski[49], C. Trigilio[36], I. S. Troitsky[34], and G. Umana[36]

[1] Kavli Institute for Particle Astrophysics and Cosmology, SLAC National Accelerator Laboratory, Stanford University, 2575 Sand Hill Road M/S 29, Menlo Park, CA 94025, USA; mahaya@slac.stanford.edu, madejski@slac.stanford.edu
[2] Department of Astronomy, Graduate School of Science, Kyoto University, Sakyo-ku, Kyoto 606-8502, Japan
[3] University of Colorado, UCB 440, Boulder, CO 80309, USA; knalew@Colorado.edu
[4] Nicolaus Copernicus Astronomical Center, 00-716 Warsaw, Poland; sikora@camk.edu.pl
[5] Space Science Institute, Boulder, CO 80301, USA
[6] Infrared Processing and Analysis Center, California Institute of Technology Pasadena, CA 91125, USA
[7] Max-Planck Institut für Extraterrestrische Physik, 85748 Garching, Germany
[8] Department of Physics, Stockholm University, AlbaNova, SE-106 91 Stockholm, Sweden
[9] The Oskar Klein Centre for Cosmoparticle Physics, AlbaNova, SE-106 91 Stockholm, Sweden
[10] Department of Astronomy, Stockholm University, SE-106 91 Stockholm, Sweden
[11] Department of Physical Sciences, Hiroshima University, Higashi-Hiroshima, Hiroshima 739-8526, Japan
[12] Institute of Space and Astronautical Science, JAXA, 3-1-1 Yoshinodai, Chuo-ku, Sagamihara, Kanagawa 252-5210, Japan
[13] Astronomical Observatory, Jagiellonian University, 30-244 Kraków, Poland
[14] Cahill Center for Astronomy and Astrophysics, California Institute of Technology, Pasadena, CA 91125, USA
[15] Agenzia Spaziale Italiana (ASI) Science Data Center, I-00044 Frascati (Roma), Italy
[16] Dipartimento di Fisica, Università degli Studi di Perugia, I-06123 Perugia, Italy
[17] NASA Goddard Space Flight Center, Greenbelt, MD 20771, USA
[18] Institut für Astro- und Teilchenphysik and Institut für Theoretische Physik, Leopold-Franzens-Universität Innsbruck, A-6020 Innsbruck, Austria
[19] Istituto Nazionale di Fisica Nucleare, Sezione di Perugia, I-06123 Perugia, Italy
[20] Hiroshima Astrophysical Science Center, Hiroshima University, Higashi-Hiroshima, Hiroshima 739-8526, Japan
[21] Department of Physics and Astrophysics, Nagoya University, Chikusa-ku, Nagoya 464-8602, Japan
[22] Dark Cosmology Centre, Niels Bohr Institute, University of Copenhagen, 2100 Copenhagen, Denmark
[23] Thuringer Landessternwarte Tautenburg, D-07778 Tautenburg, Germany
[24] International Centre for Radio Astronomy Research and Curtin University of Technology, Bentley, WA 6845, Australia
[25] CSIRO Astronomy and Space Science P.O. Box 76, Epping, NSW 1710, Australia
[26] INAF, Osservatorio Astronomico di Torino, I-10025 Pino Torinese (TO), Italy
[27] Instituto de Astrofísica de Andalucía, CSIC, E-18080 Granada, Spain
[28] Institute for Astrophysical Research, Boston University, Boston, MA 02215, USA
[29] Department of Astronomy, University of Michigan, Ann Arbor, MI 48109-1090, USA
[30] Pulkovo Observatory, 196140 St. Petersburg, Russia
[31] Max-Planck-Institut für Radioastronomie, Auf dem Hügel 69, 53121 Bonn, Germany
[32] Instituto de Astronomía, Universidad Nacional Autónoma de México, México, D. F., Mexico
[33] Tuorla Observatory, Department of Physics and Astronomy, University of Turku, FI-21500 Piikkiö, Finland
[34] Astronomical Institute, St. Petersburg State University, St. Petersburg, Russia
[35] Astrophysical Institute Department of Physics and Astronomy, Ohio University, Athens, OH 45701, USA
[36] INAF, Osservatorio Astrofisico di Catania, 95123 Catania, Italy
[37] EPT Observatories, Tijarafe, La Palma, Spain
[38] INAF, TNG Fundacioń Galileo Galilei, La Palma, Spain
[39] Graduate Institute of Astronomy, National Central University, Jhongli 32001, Taiwan
[40] INAF, Osservatorio Astronomico di Roma, I-00040 Monte Porzio Catone (Roma), Italy
[41] INAF, Osservatorio Astronomico di Collurania "Vincenzo Cerruli," 64100 Teramo, Italy
[42] Agrupació Astronòmica de Sabadell, 08206 Sabadell, Spain
[43] Harvard-Smithsonian Center for Astrophysics, Cambridge, MA 02138, USA
[44] ZAH, Landessternwarte, Universität Heidelberg, Königstuhl, D 69117 Heidelberg, Germany
[45] Instituto de Astronomía, Universidad Nacional Autónoma de México, Ensenada, B. C., Mexico
[46] School of Cosmic Physics, Dublin Institute for Advanced Studies, Dublin 2, Ireland
[47] Abastumani Observatory, Mount Kanobili, 0301 Abastumani, Georgia
[48] Department of Physics, National Taiwan University, 106 Taipei, Taiwan
[49] Aalto University Metsähovi Radio Observatory, FIN-02540 Kylmälä, Finland
[50] Isaac Newton Institute of Chile, St. Petersburg Branch, St. Petersburg, Russia
[51] School of Physics and Astronomy, University of Southampton, Highfield, Southampton, SO17 1BJ, UK
[52] Finnish Centre for Astronomy with ESO (FINCA), University of Turku, FI-21500 Piikiiö, Finland
[53] Lowell Observatory, Flagstaff, AZ 86001, USA

Received 2012 February 3; accepted 2012 May 30; published 2012 July 16

ABSTRACT

We present time-resolved broadband observations of the quasar 3C 279 obtained from multi-wavelength campaigns conducted during the first two years of the *Fermi Gamma-ray Space Telescope* mission. While investigating the previously reported γ-ray/optical flare accompanied by a change in optical polarization, we found that the optical emission appears to be delayed with respect to the γ-ray emission by about 10 days. X-ray observations reveal a pair of "isolated" flares separated by ∼90 days, with only weak γ-ray/optical counterparts. The spectral structure measured by *Spitzer* reveals a synchrotron component peaking in the mid-infrared band with a sharp break at the far-infrared band during the γ-ray flare, while the peak appears in the millimeter (mm)/submillimeter (sub-mm) band in the low state. Selected spectral energy distributions are fitted with leptonic models including Comptonization of external radiation produced in a dusty torus or the broad-line region. Adopting the interpretation of the polarization swing involving propagation of the emitting region along a curved trajectory, we can explain the evolution of the broadband spectra during the γ-ray flaring event by a shift of its location from ∼1 pc to ∼4 pc from the central black hole. On the other hand, if the γ-ray flare is generated instead at sub-pc distance from the central black hole, the far-infrared break can be explained by synchrotron self-absorption. We also model the low spectral state, dominated by the mm/sub-mm peaking synchrotron component, and suggest that the corresponding inverse-Compton component explains the steady X-ray emission.

Key words: galaxies: active – galaxies: jets – gamma rays: galaxies – quasars: individual (3C 279) – radiation mechanisms: non-thermal – X-rays: galaxies

Online-only material: color figures

1. INTRODUCTION

Blazars are active galactic nuclei characterized by highly luminous and rapidly variable continuum emission at all observed bands. The most commonly accepted scenario has their broadband emission Doppler-boosted by a relativistic jet pointing close to our line of sight (e.g., Ulrich et al. 1997). While the jet emission usually dominates the observed broadband spectrum, the optical/ultraviolet (UV) and infrared (IR) spectra often also reveal signatures of the central engine: broad emission lines, and in some cases, quasi-thermal optical/UV emission and IR dust emission, indicating the presence of an accreting supermassive black hole. Most viable current models for the origin of such jets involve conversion of the gravitational energy of matter flowing onto the black hole to the kinetic energy of the relativistic outflow or tapping the rotation energy of a spinning black hole. However, the conversion process itself is not well understood, and many additional questions regarding the dissipation region of the jet's energy into radiation and, in particular, its location remain unanswered.

Major advances in understanding blazars came as a result of the discovery by the EGRET instrument on board the *Compton Gamma-Ray Observatory* (*CGRO*) that they are strong γ-ray emitters, with γ-rays dominating radiative output (Hartman et al. 1999). With this, multi-band observations, including the γ-ray band, hold the promise of answering many outstanding questions regarding the structure of the relativistic jets of blazars.

3C 279 ($z = 0.536$; Lynds et al. 1965) is in fact one of the first γ-ray blazars discovered by EGRET in 1991 (Hartman et al. 1992). The γ-ray signal had been significantly detected in each observation by EGRET since its discovery (see, e.g., Hartman et al. 2001a), with the flux having ranged over roughly two orders of magnitude, from $\sim 10^{-7}$ up to $\sim 10^{-5}$ photons cm^{-2} s^{-1} above 100 MeV (Maraschi et al. 1994; Wehrle et al. 1998), and a factor of two variation on timescales as short as 8 hr. The photon index in the EGRET γ-ray band ranged from 1.8 to 2.3 (Nandikotkur et al. 2007). On a few occasions, 3C 279 was also detected at lower energies by *CGRO*'s OSSE (50 keV–1 MeV; McNaron-Brown et al. 1995) and COMPTEL (0.75–30 MeV; Hermsen et al. 1993; Collmar et al. 2001) instruments, indicating that the γ-ray emission forms a broad peak in the νF_ν representation. In 2008 July, the *AGILE* satellite observed a γ-ray flare associated with the source with 11.1σ significance (Giuliani et al. 2009), with an average flux above 100 MeV of $(21.0 \pm 3.8) \times 10^{-7}$ photons cm^{-2} s^{-1} and the photon index of 2.22 ± 0.23 between 100 and 1000 MeV. In the very high energy (VHE) γ-ray regime above 100 GeV, the imaging atmospheric Cherenkov telescope MAGIC detected flares twice in 2006 February (Albert et al. 2008) and in 2007 January (Aleksić et al. 2011), which made this source the most distant currently known VHE γ-ray emitter.

Optical and UV observations of the source in relatively low states—when the jet emission was relatively faint—allowed a study of the accreting black hole and the associated accretion disk. The luminosity of the accretion disk was estimated to be $L_D \sim 2 \times 10^{45}$ erg s^{-1} (Pian et al. 1999). The mass of central supermassive black hole was estimated to be in the range of $(3\text{–}8) \times 10^8\, M_\odot$ using the luminosity of optical broad line (Woo & Urry 2002) or the H_β line width (Gu et al. 2001). Those values are similar to the estimates based on the luminosity of the host galaxy (Nilsson et al. 2009).

3C 279 contains a compact radio core, associated with time-variable jet-like structure. Radio observations at 43 GHz by Very Long Baseline Array (VLBA) between 1998 March and 2001 April revealed superluminal motion of the jet with apparent speeds that range from $5c$ to $17c$ (Jorstad et al. 2004, 2005). Those observations also allowed an estimate of the Lorentz factor of the jet flow of $\Gamma_j = 15.5 \pm 2.5$ and of the viewing angle of the jet $\Theta_0 = 2\overset{\circ}{.}1 \pm 1\overset{\circ}{.}1$, corresponding to a Doppler beaming factor of $\delta = 24.1 \pm 6.5$. A change of the trajectory of a jet component has also been reported in radio observations with VLBA (Homan et al. 2003). Those authors estimated the jet component to be moving with a Lorentz factor $\Gamma_j \gtrsim 15$ at an initial viewing angle of $\lesssim 1^\circ$.

The broadband spectral energy distribution (SED) of the source is characterized by a two-bump structure, similar to many other γ-ray blazars. In the context of widely accepted

leptonic models, the lower-frequency bump, peaking at the far-IR and extending to the extreme UV band, is commonly ascribed to synchrotron radiation from relativistic electrons in the jet. The second bump, spanning from the X-ray to the γ-ray band with a peak in the MeV–GeV range, is believed to be generated via inverse-Compton scattering, presumably by the same population of particles that radiate at lower energies via the synchrotron process. The seed photons for the Compton scattering can be synchrotron photons (synchrotron self-Compton: SSC; Maraschi et al. 1992; Bloom & Marscher 1996), accretion disk photons (external Compton scattering of direct disk radiation: ECD; Dermer et al. 1992; Dermer & Schlickeiser 1993) and accretion disk photons re-scattered by the broad-line region clouds/intercloud medium (ECC; Sikora et al. 1994; Blandford & Levinson 1995), or infrared radiation from a torus located beyond the broad-line region (ERC-IR; Sikora et al. 1994). Specific to 3C 279, multi-wavelength snapshot observations for several epochs including γ-rays were presented in Hartman et al. (2001a). Those authors explained the overall spectra using the leptonic model, where the X-ray photons are mainly produced by SSC, and both ECD and ECC contribute to the γ-ray emission. Spectral variability was explained by variations of the bulk Lorentz factor of the jet, accompanied by changes in the spectral shape of the electron distribution.

The optical variability of 3C 279 is extreme: in 1937, it showed optical (B) magnitude of 11.27 (Eachus & Liller 1975), making it one of the most luminous active galaxies ever recorded. The strong variability recorded in all bands provides an opportunity to establish the relationship between emission in those bands, and thus can be used to constrain theoretical models of physical regions of the jet responsible for such emission. Many such multi-wavelength campaigns have been conducted (see, e.g., Maraschi et al. 1994; Wehrle et al. 1998; Larionov et al. 2008; Collmar et al. 2010), but they have not revealed a simple relationship between the variability in various bands: radiation in different spectral regimes does not always rise and fall simultaneously, although the periods of increased rapid activity in all bands seem to last for several months, and take place when the source is relatively bright. A recent paper by Chatterjee et al. (2008) presents the results of the monitoring of 3C 279 for 11 years in radio, optical, and X-rays, and discusses the details of the jet structure based on multi-band correlation studies. However, due to the lack of deployed instruments, long-term monitoring observations could not include the γ-ray regime, where the source often shows stronger variability than in other bands.

The launch of the *Fermi Gamma-ray Space Telescope* on 2008 June 11 has rejuvenated multi-band studies of blazars. The Large Area Telescope (LAT; Atwood et al. 2009) instrument on board *Fermi* can monitor all γ-ray sources on the sky with its a wide field of view and a much larger effective area compared to earlier γ-ray missions. Taking advantage of this new instrument for γ-ray observations, we have organized intensive multi-wavelength campaigns for 3C 279 from radio to the high-energy γ-ray energy ranges. Many ground-based telescopes (cm, mm, near-IR, and optical) and various satellites (IR, UV, X-ray, hard X-ray, and high-energy γ-ray) participated in this campaign. We reported the first results of the campaign in Abdo et al. (2010b, hereafter Paper I), where we discovered the dramatic change of the optical polarization coincident with the γ-ray flare. Here, we provide details of the multi-band observations and the interpretation of those data for the two-year interval between 2008 August and 2010 August. In Section 2, we present and briefly discuss the features of the LAT γ-ray data; in Section 3, we present the data in lower energy bands. Section 4 highlights the features of time series measured in various bands including their cross-correlations, and the general properties of the broadband SED. In Section 5, we provide viable emission models for the source in the context of leptonic scenarios.

2. *FERMI*-LAT DATA AND RESULTS

Fermi-LAT is a pair-production telescope with large effective area (8000 cm^2 on axis at 1 GeV for the event class considered here), and large field of view (2.4 sr at 1 GeV), sensitive to γ-rays in the energy range from 20 MeV to >300 GeV. Information regarding on-orbit calibration procedures is given in Abdo et al. (2009a). *Fermi*-LAT normally operates in a scanning "sky-survey" mode, which provides a full-sky coverage every two orbits (3 hr). For operational reasons, the standard rocking angle (defined as the angle between the zenith and the center of the LAT field of view) for survey mode was increased from 35° to 50° on 2009 September 3.

2.1. Observation and Data Reductions

The data used here comprise two-year observations obtained between 2008 August 4 and 2010 August 6 (MJD 54682–55414). We used the standard LAT analysis software, *ScienceTools v9r21*. The events were selected using so-called diffuse class events. In addition, we excluded the events with zenith angles greater than 100° to avoid the contamination of the Earth-limb secondary γ radiation. The events were extracted in the range between 200 MeV and 300 GeV within a 15° acceptance cone of the region of interest (ROI) centered on the location of 3C 279 (R.A. = 195.°047, decl. = −5.°789, J2000). Below 200 MeV, the effective collection area of LAT for the diffuse class events drops very quickly and thus larger systematic errors are expected. The γ-ray flux and spectrum were calculated using the instrument response function (IRF) of "P6_V11_DIFFUSE" by an unbinned maximum likelihood fit of model parameters. We examined the significance of the γ-ray signal from the sources by means of the test statistic (TS) based on the likelihood ratio test.[54] The background models included a component for the Galactic diffuse emission along the plane of the Milky Way, which was modeled by the map cube file "*gll_iem_v02_P6_V11_DIFFUSE.fits*." An isotropic component (*isotropic_iem_v02_P6_V11_DIFFUSE.txt*) was also included to represent the extragalactic diffuse emission and residual instrumental background. Besides those components, the model in our analysis also included the emission from all nearby point sources inside the ROI from the first *Fermi*-LAT catalog (1FGL: Abdo et al. 2010c). The spectra of those sources were modeled by power-law functions except for a pulsar 1FGL J1231.1–1410 (=PSR J1231–1411), for which we included an additional exponential cutoff in its spectral modeling. During the spectral fitting, the normalization factors of the Galactic diffuse and isotropic components and the nearby sources were left as free parameters, and the photon indices of the nearby sources were fixed to the values from the 1FGL catalog except for 3C 273, whose photon index was allowed to vary freely. In the light curve analysis, we considered only two bright sources in the background model as nearby point sources, namely, 3C 273

[54] TS = 25 with two degrees of freedom corresponds to an estimated ∼4.6σ pre-trials statistical significance assuming that the null-hypothesis TS distribution follows a χ^2 distribution (see Mattox et al. 1996).

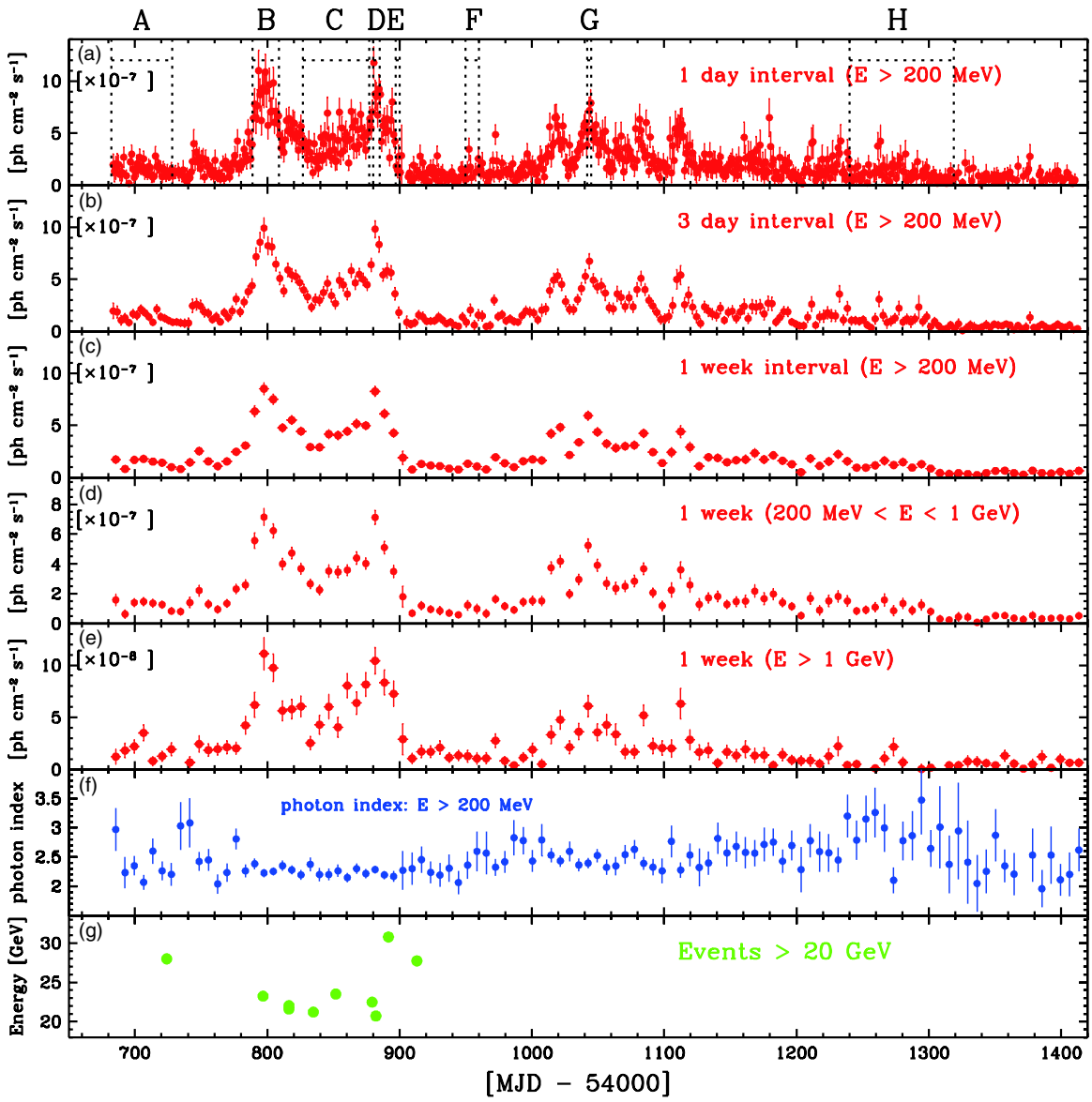

Figure 1. Gamma-ray light curves of 3C 279 during the first two years of the *Fermi*-LAT observations from 2008 August to 2010 August, plotted in (a) one day intervals at energies above 200 MeV, (b) three day intervals at energies above 200 MeV, (c) one week intervals at energies above 200 MeV, (d) one week intervals at energies between 200 MeV and 1 GeV, (e) one week intervals at energies above 1 GeV. The panel (f) shows the history of the photon index at energies above 200 MeV in one week intervals, while the panel (g) shows arrival time distribution of >20 GeV events associated with 3C 279. The vertical axis of the panel (g) represents the estimated energy of events. The highest energy photon corresponds to 30.8 GeV at MJD 54891. The dotted lines and capital letters represent time intervals where γ-ray spectra are extracted (see also Table 1).

(A color version of this figure is available in the online journal.)

and 1FGL J1231.1–1410, because other nearby sources had a negligible contribution to γ-ray signal, especially in such relatively short timescales (shorter than a week) for the light curves considered here. The fluxes used for the light curve were calculated by a simple power-law model fit using data in the given energy ranges.

2.2. Temporal Behavior

The γ-ray light curve measured by *Fermi*-LAT can be seen in Figure 1. The figure shows the flux history above 200 MeV averaged over (a) one day intervals, (b) three day intervals, and (c) one week intervals. It also includes one week light curves of (d) the flux between 200 MeV and 1 GeV, (e) the flux above 1 GeV, and (f) the photon index in the range above 200 MeV.

The γ-ray flux clearly shows variability. The source showed high-flux states between MJD 54700 and 54900, in which two prominent flares can be seen: one of the flares at ∼MJD 54800 and the other at ∼MJD 54880. During the second flare, a change in the optical polarization associated with a γ-ray flare was discovered (Paper I). We detected some flux variability between MJD 55000 and 55120, but after that, the source remained in a relatively low activity state until the end of the period considered in this paper. During this two-year period, the highest integral flux above 200 MeV occurred on MJD 54880 in the one day interval light curve with flux of $F_{E>200\,\mathrm{MeV}} = (11.8 \pm 1.5) \times 10^{-7}$ photons cm^{-2} s^{-1} and TS = 306. By extrapolating the spectrum down to 100 MeV, an integral flux above 100 MeV on that day yields $F_{E>100\,\mathrm{MeV}} = (31.0 \pm 6.0) \times 10^{-7}$ photons cm^{-2} s^{-1}, which is still a factor of 3–4 times lower

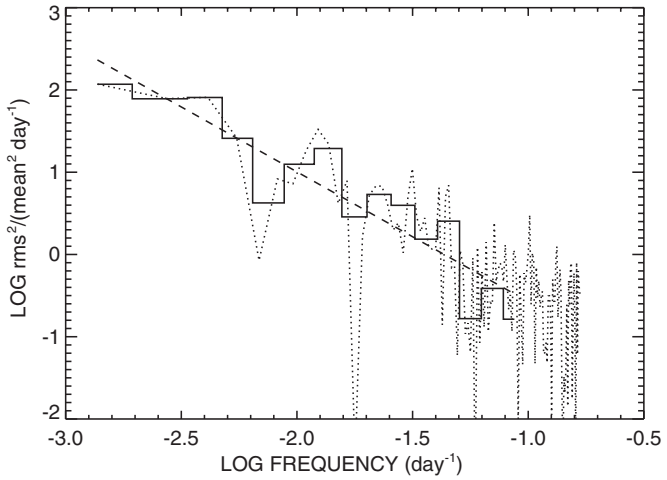

Figure 2. Power density spectrum of 3C 279 for the three day binned γ-ray light curve. The white noise level has been subtracted. The solid line histogram describes the PDS averaged in logarithmic frequency bins while the dotted curve describes the raw PDS before binning. The dashed line represents a linear fit to the binned PDS.

than the flux of the brightest flare ($\sim 1 \times 10^{-5}$ photons cm^{-2} s^{-1}) detected during the EGRET observations of the source (Wehrle et al. 1998; Hartman et al. 2001b).

We quantified the flux variability using one week interval data for energies above 200 MeV (full band), between 200 MeV and 1 GeV (soft band), and above 1 GeV (hard band). This is based on the "excess variance" method (Nandra et al. 1997; Edelson et al. 2002) after subtracting the contribution expected from measurement errors ($\sigma_{\mathrm{err},i}$). Using the mean square error $\langle \sigma_{\mathrm{err},i} \rangle$, the excess variance F_{var} can be described as (Vaughan et al. 2003)

$$F_{\mathrm{var}} = \sqrt{\frac{S^2 - \langle \sigma_{\mathrm{err},i} \rangle^2}{\langle F \rangle^2}}, \quad (1)$$

where S is the variance of the flux, and $\langle F \rangle$ is the mean value of the flux. The definition of associated error can be found in Vaughan et al. (2003). In the calculation, we excluded bins of 8, 82, 87, and 90 because the fit in the hard band failed due to poor statistics of the data samples. Resulting F_{var} values are 0.695 ± 0.015, 0.648 ± 0.017, and 0.839 ± 0.030 for the full, soft, and hard bands, respectively. The resulting values indicate that the flux of the hard band showed significantly stronger variability than that of the soft band. For comparison, $F_{\mathrm{var}} = 0.79 \pm 0.02$ for $E > 300$ MeV has been reported during the first 11 months of the *Fermi* scientific mission (Abdo et al. 2010f), when the source has clearly been more active.

A power density spectrum (PDS) for the three day binned light curve was calculated using a Fourier transform and is shown in Figure 2. The power density was normalized to fractional variance per frequency unit (rms^2 I^{-2} day^{-1}) and the PDS points were averaged in logarithmic frequency bins. The white noise level was estimated from the rms of the flux errors and was subtracted from the PDS. A slope of 1.6 ± 0.2 was obtained from a linear fit to the binned PDS for frequencies up to 0.1 day^{-1}. The main uncertainty in the estimated PDS slope is due to the stochastic nature of the variability which leads to variations in the determined slope between different time-limited observations. An additional effect which can cause a systematic bias in the observed PDS slope is the red noise leakage (e.g., Chatterjee et al. 2008). In the present analysis this effect is not taken into account.

Figure 3 shows plots of flux versus photon index (Γ) based on the weekly light curve results above 200 MeV (full band), between 200 MeV and 1 GeV (soft band), and above 1 GeV (hard band). The data that have TS > 10 were selected for the plots and are shown in gray points. An average photon index was calculated by fitting a constant value in each plot, corresponding to $\Gamma_{>200\,\mathrm{MeV}} = 2.334 \pm 0.015$, $\Gamma_{200\,\mathrm{MeV}-1\,\mathrm{GeV}} = 2.20 \pm 0.03$, and $\Gamma_{>1\,\mathrm{GeV}} = 2.48 \pm 0.04$ for the full, soft, and hard bands, respectively. The average photon index in the soft band shows a significantly harder spectrum than that in the hard band.

We also derived photon indices resulting from an analysis where the data were sorted in five bins using week-long fluxes for each energy band, and plotted the results as red points. Those photon indices of each flux bin are also shown in the insets in Figure 3. For the full band, although the change of the photon index is rather small ($\Delta\Gamma \sim 0.2$) compared to the flux variation (spanning about an order of magnitude), a weak "harder when brighter" effect can be seen. Such an effect was also measured in other LAT blazars (Abdo et al. 2010e). The soft band also shows the weak "harder when brighter" effect with a slightly larger change of the photon index ($\Delta\Gamma \sim 0.4$). On the other hand, the photon index of the hard band changes only sightly ($\Delta\Gamma \sim 0.1$) and is statistically consistent with a constant value.

2.3. Highest Energy Photons

During the two year observations, the highest energy photon associated with 3C 279 was detected at MJD 54891.60745 with an estimated energy of 30.8 GeV. The event was converted in the front-thin layers (so-called front event) of the LAT detector and still remains even when we apply the cleanest event selection (so-called data clean event), which was developed for studying extragalactic γ-ray background (Abdo et al. 2010g). The reconstructed arrival direction of the event is $5\farcm7$ ($= 0\fdg095$) away from 3C 279, and is within the 68% containment radius of the LAT point-spread function (PSF; $0\fdg114$ in the IRF of "P6_V11_DIFFUSE") for front events at 30.8 GeV. Based on our model fit of the epoch which contains that highest energy photon, we find the probability that the photon was associated with 3C 279 (as opposed to all other sources in the model including the diffuse emission and nearby point sources) is 88.6%.

In total, we found 10 events with estimated energies higher than 20 GeV within an $0\fdg25$ radius centered at 3C 279. All events lie within a 95% containment radius of the LAT PSF from 3C 279 and remain even after the "data clean selection" applied. The number of expected background events above 20 GeV within the $0\fdg25$ radius at the location of 3C 279 for the two year observations is only 0.16 events. The bottom panel of Figure 1 plots the arrival time distribution of those 10 events. All events except for two were detected between MJD 54780 and 54900 during the high-activity states. No photon above 20 GeV associated with 3C 279 has been detected after MJD 54914 during the two year observations.

2.4. Gamma-Ray Spectra

We extracted the γ-ray spectra using data for the entire two-year period and following eight sub-periods (see also Table 1): (A) the initial quiescent state in the γ-ray band (MJD 54682–54728), (B) the first γ-ray flaring state (MJD 54789–54809), (C) an intermediate state (MJD 54827–54877),

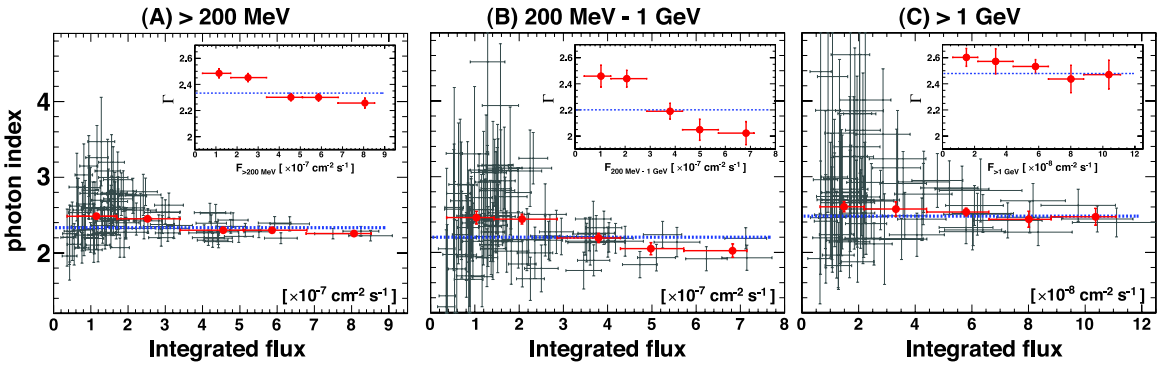

Figure 3. Plots of the integrated γ-ray flux vs. photon index of 3C 279 measured in week-long bins for energies above 200 MeV (A), between 200 MeV and 1 GeV (B), and above 1 GeV (C). Only points with TS $>$ 10 are plotted (gray points). The blue dotted horizontal lines indicate average photon indices of those data for each energy band. Red points show the photon indices resulting from an analysis where the data were sorted in five bins using week-long fluxes for each energy band. For the red points, the horizontal bars indicate the ranges of the week-long flux bins while the vertical bars indicate 1σ statistical errors. The insets show enlarged views of the red points as well as the average photon index of each energy band.

(A color version of this figure is available in the online journal.)

Table 1
Results of Spectral Fitting in the γ-Ray Band Measured by *Fermi*-LAT

Period	Gamma-Ray Spectrum (*Fermi*-LAT)						Flux ($>$100 MeV)
(MJD)	Fitting Model[a]	$\Gamma/\alpha/\Gamma_1$	β/Γ_2	$E_{\rm brk}$ (GeV)	TS	$-2\Delta L$[b]	(10^{-7} photons cm^{-2} s^{-1})
2 years	PL	2.38 ± 0.02	...	...	20272	...	6.10 ± 0.13
2008 Aug 4–2010 Aug 6	LogP	2.18 ± 0.03	0.08 ± 0.01	...	20267	46.5	5.18 ± 0.16
(54682–55414)	BPL	2.31 ± 0.02	2.95 ± 0.12	3.5 ± 0.3	20286	43.0	5.76 ± 0.15
Period A	PL	2.30 ± 0.07	...	...	797	...	3.7 ± 0.4
2008 Aug 4–2008 Sep 19	LogP	2.19 ± 0.15	0.04 ± 0.05	...	797	0.7	3.3 ± 0.5
(54682–54728)	BPL	2.21 ± 0.09	2.82 ± 0.40	3.4 ± 0.8	798	2.5	3.4 ± 0.4
Period B	PL	2.28 ± 0.04	...	...	3209	...	19.0 ± 1.1
2008 Nov 19–2008 Dec 9	LogP	1.95 ± 0.10	0.13 ± 0.04	...	3214	13.6	15.0 ± 1.3
(54789–54809)	BPL	2.00 ± 0.10	2.61 ± 0.11	1.0 ± 0.2	3215	13.7	15.8 ± 1.3
Period C	PL	2.25 ± 0.04	...	...	4107	...	10.0 ± 0.5
2008 Dec 27–2009 Feb 15	LogP	2.05 ± 0.08	0.08 ± 0.03	...	4110	8.2	8.6 ± 0.6
(54827–54877)	BPL	2.07 ± 0.08	2.43 ± 0.08	1.0 ± 0.2	4109	8.2	8.9 ± 0.6
Period D	PL	2.36 ± 0.08	...	...	1236	...	23.6 ± 2.3
2009 Feb 18–2009 Feb 23	LogP	2.16 ± 0.16	0.09 ± 0.06	...	1234	2.0	20.2 ± 2.8
(54880–54885)	BPL	2.25 ± 0.12	2.91 ± 0.61	2.3 ± 2.1	1235	2.9	21.8 ± 2.6
Period E	PL	2.64 ± 0.32	...	...	61	...	6.3 ± 2.5
2009 Mar 7–2009 Mar 10	LogP	2.64 ± 0.32	0.00 ± 0.00	...	61	0.0	6.3 ± 2.5
(54897–54900)							
Period F	PL	2.54 ± 0.24	...	...	85	...	3.5 ± 1.2
2009 Apr 29–2009 May 9	LogP	2.54 ± 0.24	0.00 ± 0.00	...	85	0.0	3.5 ± 1.2
(54950–54960)							
Period G	PL	2.44 ± 0.13	...	...	460	...	18.8 ± 2.9
2009 Jul 30–2009 Aug 2	LogP	2.37 ± 0.25	0.03 ± 0.10	...	460	0.1	17.7 ± 4.0
(55042–55045)							
Period H	PL	2.83 ± 0.11	...	...	398	...	3.7 ± 0.5
2010 Feb 13–2010 May 3	LogP	2.56 ± 0.23	0.16 ± 0.13	...	399	1.9	2.9 ± 0.6
(55240–55319)	BPL	2.72 ± 0.43	3.47 ± 0.57	1.6 ± 0.5	399	1.6	3.4 ± 1.7

Notes.
[a] PL: power-law model; LogP: log parabola model; BPL: broken power-law model. See definitions in the text.
[b] ΔL represents the difference of the logarithm of the likelihood of the fit with respect to a single power-law fit.

(D) the first five days of the second γ-ray flaring event (MJD 54880–54885), (E) the last three days of the second γ-ray flaring event (MJD 54897–54900), (F) during the isolated (first) X-ray flaring event (MJD 54950–54960; see Section 4), (G) during the second X-ray flaring event (MJD 55042–55045; see Section 4), and (H) a quiescent state (MJD 55240–55319). Those sub-periods were also selected taking into account observations in other energy bands. SEDs in the γ-ray band for each sub-period are presented in Figure 4. Each γ-ray spectrum was modeled using a simple power-law (PL; $dN/dE \propto E^{-\Gamma}$), a broken power-law (BPL; $dN/dE \propto E^{-\Gamma_1}$ for $E < E_{\rm brk}$ and $dN/dE \propto E^{-\Gamma_2}$ otherwise), and a log parabola (LogP; $dN/dE \propto (E/E_0)^{-\alpha-\beta\log(E/E_0)}$) model. In the case of LogP model, the parameter β represents the curvature around the

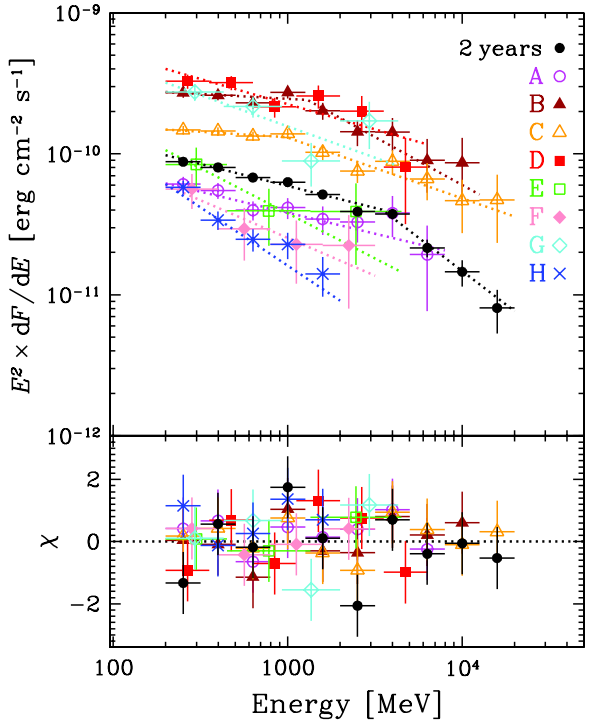

Figure 4. Gamma-ray spectral energy distributions of 3C 279 of each period as defined in the text or Table 1. Two-year averaged (black filled circles), Period A (magenta open circles), Period B (brown filled triangles), Period C (orange open triangles), Period D (red filled squares), Period E (green open squares), Period F (pink filled diamonds), Period G (cyan open diamonds), and Period H (blue crosses). The vertical bars indicate 1σ statistical errors while the horizontal bars indicate energy ranges of each bin. The best-fit spectral models are plotted as dotted lines for each period and their parameters are summarized in Table 1. We use the broken power-law model for the spectra of two years, Period B, and Period C because significant improvements in the spectral fits can be seen compared to the simple power-law model (see Table 1) while the simple power-law model is used for other periods. The lower panel shows the residuals, plotted as χ ($\equiv$ (data − model)/data error) from the best-fit models. A "dip" feature at ∼1–2 GeV in the spectrum of Period G (the third point in cyan) is a $\leqslant 2\sigma$ effect from the best-fit model, thus not statistically significant.

(A color version of this figure is available in the online journal.)

peak. We note that the choice of the reference energy E_0 in the LogP model does not affect the determination of the other two model parameters, and hence we fixed it at 300 MeV.

The best-fit parameters calculated by the fitting procedure are summarized in Table 1. The integral fluxes above 100 MeV[55] derived using each spectral model are also included. The averaged γ-ray spectral shape for the two year observation significantly deviates from a single power law. A LogP model is favored to describe the γ-ray spectral shape over the simple PL model with the difference of the logarithm of the likelihood fits[56] $-2\Delta L = 46.5$ (corresponding to a significance level of $\sim 7\sigma$),[57] and a BPL fit yields $-2\Delta L = 43.0$. Even in some individual periods as defined above, the spectra deviate from a single power law: for example, the spectrum in the Period B yields $-2\Delta L = 13.6$. This is consistent with our finding in Section 2.2 that the spectrum above 1 GeV is significantly softer than the spectrum below 1 GeV. We thus conclude that the γ-ray spectrum significantly deviates from a simple power law. The spectral break in 3C 279 is not as pronounced as that seen in the spectra, e.g., of 3C 454.3 (Ackermann et al. 2010). One the other hand, the BPL model returns break energies within a few GeV range regardless of the flux levels as observed in other bright FSRQs, such as 3C 454.3 and 4C+21.35 (Tanaka et al. 2011). Such a spectral feature could be due to γ–γ absorption to pair production by He II Lyman recombination continuum UV photons from the emission line region (see, e.g., Poutanen & Stern 2010), or a break in the electron distribution (Abdo et al. 2009b). We consider the γ-ray emission region to be located significantly beyond the broad emission region (see the Discussion in Section 5), and this implies that the break in the electron energy distribution is the more likely explanation.

[55] Although we use photon data from 200 MeV, the integral fluxes are extrapolated down to 100 MeV, which is convenient to compare with other γ-ray results.

[56] $-2\Delta L = -2\log(L0/L1)$, where $L0$ and $L1$ are the maximum likelihood estimated for the null and alternative hypothesis, respectively.

[57] Because the LogP model has one more free parameter than the PL model has, the $-2\Delta L$ distribution follows a χ^2 distribution with one degree of freedom.

3. MULTI-WAVELENGTH OBSERVATIONS AND DATA REDUCTION

3.1. X-Ray and Hard X-Ray: Suzaku

The *Suzaku* X-ray satellite (Mitsuda et al. 2007) observed 3C 279 as a part of multi-band studies of the object. The observations took place in two segments, with an interruption lasting roughly 1.5 days: (1) between 2009 January 19, 23:19:00 and 2009 January 22, 22:32:00 UTC (sequence number 703049010), and (2) between 2009 January 23, 20:45:00 and 2009 January 25, 03:00:00 UTC (sequence number 703049020). "Period C" (see Table 1) includes both *Suzaku* observations. The goals of the *Suzaku* observations were to monitor the soft-medium X-ray flux (0.3–12 keV) of the source with the X-ray Imaging Spectrometer (XIS; Koyama et al. 2007) and to take advantage of the data from the Hard X-ray Detector (HXD; Takahashi et al. 2007). The HXD consists of PIN silicon diodes for the lower energy band (10–70 keV) and GSO scintillators for the higher energy band (40–600 keV), to extend the spectral bandpass beyond the energies accessible with imaging instruments (>10 keV). The HXD nominal position was used for the observations to maximize its effective area. In the following analysis, the HXD/GSO data were not used because there was no significant detection of the source.

Although the observation conditions were nominal, the XIS1 data suffered from somewhat high and variable background, resulting in the total apparent counting rate ranging from one to three counts s^{-1} in source-free regions for the entire chip. Still, the background-subtracted spectrum determined from the XIS1 data below 8 keV was entirely consistent with that from XIS0 and XIS3 and thus we included the background-subtracted XIS1 data in the spectral fitting. The total duration of good data accumulated by the XIS instruments was 191 ks. We used the standard `ftools` data reduction package, provided by the *Suzaku* Science Operations Center, with the calibration files included in CALDB ver. 4.3.1. For the analysis of spectra and light curves, we extracted the counts from a region corresponding to a circle with 260″ radius, centered on the X-ray centroid; we used a region of a comparable size from the same chip to extract the background counts. The net count rates were 0.47, 0.63, and 0.56 count s^{-1} for XIS0, XIS1, and XIS3, respectively, with the typical count rate uncertainty in the entire observations of ∼3%. The data indicate no significant variability during the *Suzaku* observations.

The source was also detected in the HXD/PIN data, although the signal was relatively weak. We used the standard cleaned events, processed using the standard criteria applicable to

the rev. 2.13 of the *Suzaku* HXD data processing software. This yielded 95.4 ks of good data, with a total count rate of 0.3 counts s^{-1}. For the background subtraction, we used the standard background files provided by the *Suzaku* team through HEASARC. We applied the standard tool `hxdpinxbpi` which accounts for the particle background as well as for the contribution of the cosmic X-ray background as appropriate for the effective area and the solid angle of the HXD. The net counting rate was 0.02 counts s^{-1}, with the formal statistical uncertainty of ∼10%. We note that this formal uncertainty is probably lower than the standard systematic error due to the background subtraction of 3% of the average background (corresponding to 0.01 counts s^{-1}). Nonetheless, even if the additional uncertainty is included, the source was still detected by the HXD/PIN.

For the spectral analysis, we used the `XSPEC` spectral analysis software. For the spectral fitting of the XIS data, we used the standard redistribution files and mirror effective areas generated with *Suzaku*-specific tools `xisrmfgen` and `xissimarfgen`. In the spectral fits, we used the counts corresponding to the energy range of 0.5–10.0 keV for XIS0 and XIS3, and 0.5–8.0 keV for the XIS1. We used all three XIS detectors simultaneously, but allowed for a small (a few %) variation of normalization. For the HXD/PIN data, we considered the data in the range of 20–50 keV and used the response file `ae_hxd_pinhxnome5_20080716.rsp`.

The source spectrum was modeled as an absorbed power law, with the cross-sections and elemental abundances as given in Morrison & McCammon (1983); other absorption models give similar results. The best-fit absorbing column was $(3.1 \pm 0.5) \times 10^{20}$ cm^{-2}, and the photon index was 1.76 ± 0.01. Inclusion of the HXD/PIN data in the fit did not change the fit parameters perceptibly. The χ^2 for the fit including the three XIS detectors and the HXD/PIN was acceptable, with 5061 for 5023 channels. The absorption inferred from the simple absorbed power-law model is marginally greater than the value inferred from the radio measurements of the column density of the material in the Galaxy of 2.0×10^{20} cm^{-2} (with an estimated error of ∼10%; Kalberla et al. 2005). We deem the difference not significant, since at such small column densities, it can be accounted for by even small systematic uncertainty in the knowledge of the effective area of the XIS instruments at the lowest end of the XIS bandpass. Furthermore, a modest additional column density is expected in the host galaxy of 3C 279. The observed model 2–10 keV flux is 8.0×10^{-12} erg cm^{-2} s^{-1}, with the statistical error of <2%, which is probably smaller than the systematic error resulting form the calibration uncertainty of the *Suzaku* instruments. We plot the *Suzaku* 3C 279 spectra in Figure 5.

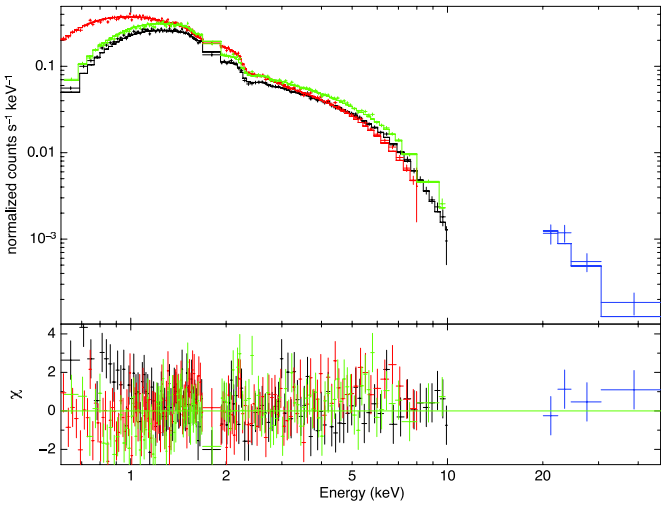

Figure 5. Count spectra of 3C 279 measured by *Suzaku* XIS0 (black), XIS1(red), XIS3 (green), and HXD/PIN (blue). The model plotted with the data is a broken power law obtained by fitting these three XISs and HXD/PIN data. The lower panel shows the residuals for this broken power-law model.

(A color version of this figure is available in the online journal.)

3.2. X-Ray: XMM-Newton

XMM-Newton observed 3C 279 once starting on 2009 January 21, 17:28 UT. The observation was largely devoid of flares (except for the period close to the end of the observation), and the total length of good data accumulated in the pointing was 16.8 ks. We used the standard Scientific Analysis System (SAS) data reduction package, provided by the *XMM-Newton* Science Operations Center. Since 3C 279 is a relatively bright source, we considered only the pn-CCD data. We note here that the spectra and light curves taken by MOS-CCDs were entirely consistent with the results inferred from the pn-CCD data.

For the analysis of spectra and light curves, we extracted the counts from within 40″ radius of the source; we used a region of the same size, from the same pn-CCD chip, to extract the background counts. The data indicate no significant variability during the *XMM-Newton* observation. The spectral analysis was performed using the `XSPEC` v.12 spectral analysis software with the standard redistribution files and mirror effective areas included in the SAS package. We used the counts corresponding to the energy range of 0.5–10.0 keV in our spectral fits.

The source spectrum was first modeled as an absorbed power law; the best-fit absorbing column was $(2.2 \pm 0.6) \times 10^{20}$ cm^{-2}, and the photon index was 1.77 ± 0.03, with χ^2 of 588 for 517 dof. The result is consistent with the spectral analysis results of the *Suzaku* observations as described in the previous section, which were performed during the same period as the *XMM-Newton* observation. We also considered a broken power-law model and found that the overall intrinsic source spectrum hardens with increasing energy. The absorbing column was $(3.4 \pm 0.7) \times 10^{20}$ cm^{-2}, and the low- and high-energy indices were, respectively, 1.83 ± 0.05 and 1.55 ± 0.2 with the break energy of 4.1 ± 0.8 keV. The resulting χ^2 was 563, for 515 dof. The broken power-law model is statistically only marginally superior to the simple power-law model, especially given that the absorption inferred form the simple power-law model is closer to the value inferred from Kalberla et al. (2005). For either model, the 2–10 keV flux is 7.7×10^{-11} erg cm^{-2} s^{-1}, with a statistical error of 5%, which is probably smaller than the systematic error resulting form the calibration uncertainty of the *XMM-Newton* pn-CCD.

3.3. X-Ray: RXTE-PCA

RXTE carried out 321 observations between 2008 July 3 (MJD 54650) and 2010 August 12 (MJD 55420). Those include 52 observations based on the Cycle 12 Guest observer (GO) program and 269 observations based on the Core program in Cycles 12–14. The fluxes resulting from the Cycle 12 GO observations have been already reported in Paper I. Most of the individual observations have exposure times in a range from 1.0 to 2.5 ks. We analyzed the data from the Proportional Counter Array (PCA) following standard procedures using the `rex` script in HEASOFT v.6.9. Only signals from the top layer (X1L and X1R) of PCU2 were extracted for data analysis. The

data were screened with the following data selection: source elevation above the horizon $>10^{\circ}$, pointing offset smaller than $0^{\circ}.02$, at least 30 minutes away from a South Atlantic Anomaly (SAA) passage and electron contamination smaller than 0.1. The background was estimated with standard procedures, and the detector response matrices were extracted with the RXTE tools (command PCARSO v.11.7.1). For the spectral analysis we re-binned the spectra into 11 channels. The spectra from the channels corresponding to nominal energies of 2.6–10.5 keV are adequately fitted by a single power-law model, absorbed by a fixed Galactic column density of 2.2×10^{20} cm^{-2} using the XSPEC v.12 software package. The value of the column density is based on our *XMM-Newton* results (in Section 3.2) and is also consistent with the value based on Kalberla et al. (2005).

3.4. X-Ray: Swift-XRT

In the HEASARC database,[58] there are 80 publicly available *Swift* X-Ray Telescope (XRT) observations between 2008 July 3 (MJD 54650) and 2010 August 12 (MJD 55420), which include 32 pointings based on an approved GI proposal in Cycle 4 (Proposal number: 5080069). The results of the flux history based on the data until 2009 May 31 have already reported in Paper I. Effective exposure times of these observations range between 1 and 3 ks, but some have longer exposure times, for example, 8.9 ks for ID:35019007 (MJD 54795), 22.5 ks for ID:35019009 (MJD 54797), 20.2 ks for ID:35019010 (MJD 54799), and 15.4 ks for ID:35019011 (MJD 54800). The XRT was used in the photon counting mode, and no evidence of pile-up was found. The XRT data were reduced with the standard software xrtpipeline v.0.12.6, applying the default filtering and screening criteria (HEADAS package, v.6.10). The source events were extracted from a circular region, 20 pixels in radius, centered on the source position. Exposure maps were used to account for PSF losses and the presence of dead pixels/columns. The background was determined using data extracted from a circular region, 40 pixels in radius, centered on (R.A., decl.: J2000) $= (12^{\rm h}56^{\rm m}26^{\rm s}, -05^{\circ}49'30'')$, where no X-ray sources are found. Note that the background contamination is less than 1% of source flux even in the faint X-ray states of the source. The data were rebinned to have at least 25 counts per bin, and the spectral fitting was performed using the energy range between 0.3 keV and 10 keV using XSPEC v.12. The Galactic column density is fixed at 2.2×10^{20} cm^{-2} during the fittings as is the case in the *RXTE* data analysis.

Figure 6 shows a scatter plot between photon index and flux in the X-ray band as measured by *Swift*-XRT and *RXTE*-PCA. Generally, a "harder-when-brighter" trend can be seen. Only the highest flux point measured by *Swift*-XRT shows the photon index significantly harder (smaller) than 1.5.

3.5. Ultraviolet: Swift-UVOT

The *Swift* Ultra-Violet/Optical Telescope (UVOT; Roming et al. 2005) data used in this analysis included all of the observations performed during the time interval MJD 54650–55420. The UVOT telescope cycled through each of the six optical and ultraviolet filters (V, B, U, $W1$, $M2$, $W2$). The UVOT photometric system is described in Poole et al. (2008). Photometry was computed from a $5''$ source region around 3C 279 using the publicly available UVOT FTOOLS data reduction suite. The background region was taken from an annulus with inner and outer radii of $27''.5$ and $35''$, respectively. Galactic absorption in the direction of 3C 279 was adapted as given in Larionov et al. (2008), namely, $A_V = 0.093$, $A_B = 0.123$, $A_U = 0.147$, $A_{W1} = 0.195$, $A_{M2} = 0.285$, and $A_{W2} = 0.271$. The measured magnitudes in each band during the two year observations are $m_V = 15.6$–18.7 (75 data points), $m_B = 16.0$–18.8 (80 data points), $m_U = 15.1$–18.0 (88 data points), $m_{W1} = 15.3$–18.0 (84 data points), $m_{M2} = 15.4$–18.2 (76 data points), and $m_{W2} = 15.5$–18.0 (81 data points). All observed data points are shown in Figure 7.

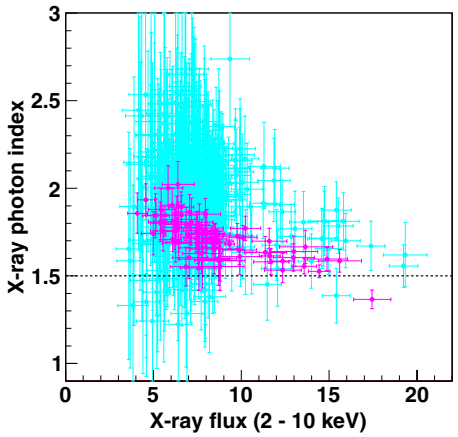

Figure 6. Scatter plot of flux vs. photon index of 3C 279 in the X-ray band with the data taken by *Swift*-XRT (magenta) and *RXTE*-PCA (cyan). The horizontal dotted line represents the photon index value of 1.5.

(A color version of this figure is available in the online journal.)

3.6. Optical, Near-infrared, and Radio Observations by GASP-WEBT

The GLAST-AGILE Support Program (GASP; Villata et al. 2008, 2009) is a project initially originating from the Whole Earth Blazar Telescope[59] (WEBT) in 2007. It is aimed to provide long-term monitoring in the optical (R band), near-IR, and mm–cm radio bands of 28 γ-ray-loud blazars during the lifetime of the *AGILE* and *Fermi* γ-ray satellites.

The observations of 3C 279 in the period considered in this paper were performed by the observatories listed in Table 2. The calibrated R-band magnitudes of the source were obtained through differential photometry with respect to the reference stars 1, 2, 3, and 5 by Raiteri et al. (1998). Near-IR data in the J, H, and K filters were acquired at Campo Imperatore and Roque de los Muchachos (Liverpool). When converting magnitudes into flux densities, optical, and near-IR data were corrected for Galactic reddening using $A_B = 0.123$ mag (Schlegel et al. 1998). We adapted the extinction laws by Cardelli et al. (1989), and the zero-mag fluxes by Bessell et al. (1998).

For the observations between 2008 August and 2010 August, the measured R-band magnitude ranged from 14.87 to 17.81 (673 data points). The R-band data have the best time coverage among the IR–optical–UV bands in our data thanks to the participation of a number of telescopes. The emission shows strong variability and the excess variance ($F_{\rm var}$; Equation (1)) of the source R-band flux (i.e., in linear scale) is 0.853 ± 0.001. The near-IR magnitudes in the J, H, and K bands were measured in ranges of $m_J = 14.91$–15.59 (20 data points), $m_H = 12.04$–14.90 (68 data points), and $m_K = 11.19$–13.45 (20 data

[58] http://heasarc.gsfc.nasa.gov/cgi-bin/W3Browse/swift.pl

[59] http://www.oato.inaf.it/blazars/webt

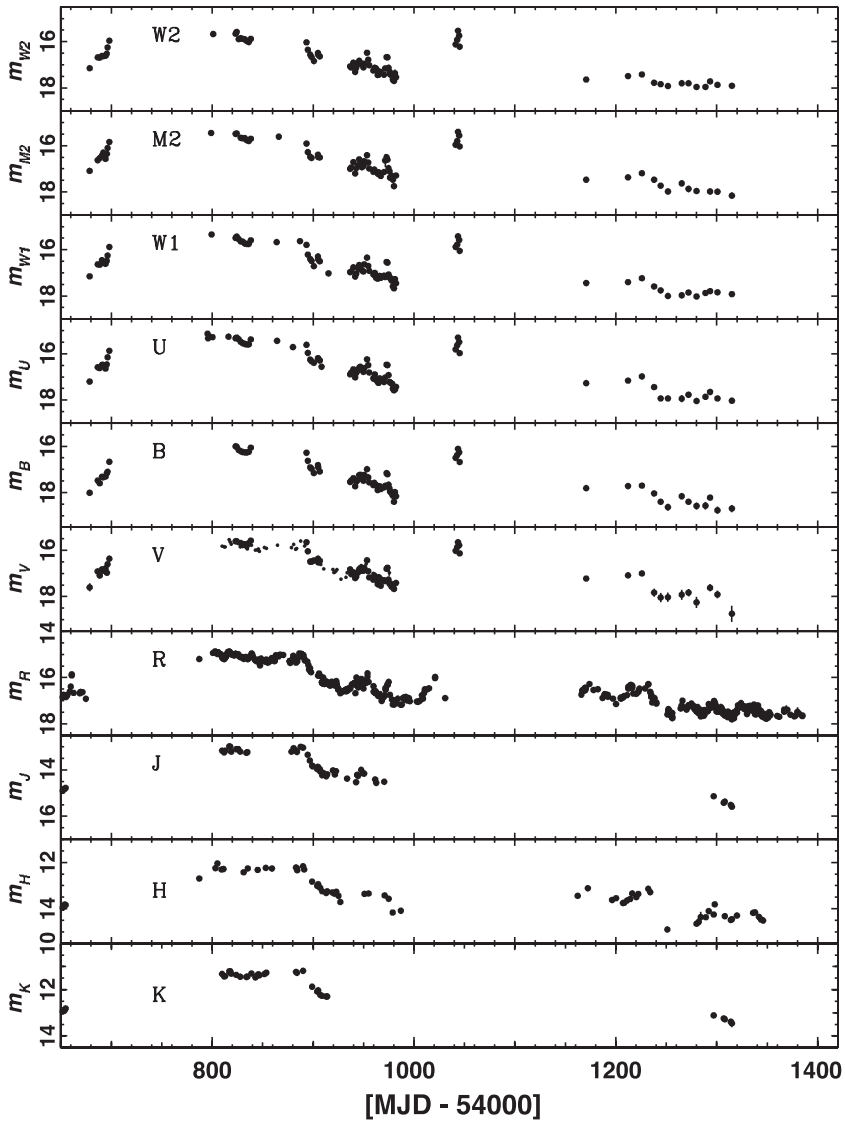

Figure 7. Light curves of all observed UV–optical–near-IR bands of 3C 279 in measured magnitude scale from 2008 August to 2010 August, including $W2$ (*Swift*-UVOT), $M2$ (*Swift*-UVOT), $W1$ (*Swift*-UVOT), U (*Swift*-UVOT), B (*Swift*-UVOT), V (Katana, *Swift*-UVOT), R (Abastumani, Calar Alto, ST-7, GRT, MDM, L'Ampolla, Perkins, SLT, KVA, LT, San Pedro, St. Petersburg, Tijarafe), J (AZT-24, Kanata), H (AZT-24, LT), and K (AZT-24, Kanata) bands.

points). Those data points are shown in Figure 7. The radio flux densities were measured in ranges of $F_{5\,\mathrm{GHz}} = 8.5$–$12.4$ Jy (109 data points), $F_{8\,\mathrm{GHz}} = 9.1$–$15.5$ Jy (124 data points), $F_{14.5\,\mathrm{GHz}} = 10.3$–$19.4$ Jy (118 data points), $F_{22\,\mathrm{GHz}} = 10$–$22$ Jy (16 data points), $F_{37\,\mathrm{GHz}} = 10$–$20$ Jy (168 data points), $F_{43\,\mathrm{GHz}} = 10$–$22$ Jy (20 data points), $F_{230\,\mathrm{GHz}} = 5.1$–$10.5$ Jy (62 data points), and $F_{345\,\mathrm{GHz}} = 6.0$–$6.8$ Jy (7 data points). The light curves of the radio flux densities in those bands are plotted in Figure 8.

3.7. Optical and Near-infrared: The Kanata Telescope

We performed the V-, J-, and Ks-band photometry and polarimetry of 3C 279 using TRISPEC installed to the 1.5 m Kanata telescope located in the Higashi–Hiroshima Observatory.

TRISPEC has a CCD and two InSb arrays, enabling photopolarimetric observations in an optical and two near-IR bands simultaneously (Watanabe et al. 2005). We obtained 64, 42 and 17 photometric measurements in the V, J, and Ks bands, respectively. A unit of the polarimetric observing sequence consisted of successive exposures at four position angles of a half-wave plates: 0°, 45°, 22.°5, 67.°5. The data were reduced according to the standard procedures of CCD photometry. We measured the magnitudes of objects with the aperture photometry technique. We performed differential photometry with a comparison star taken in the same frame of 3C 279. Its position is R.A. $= 12^{\mathrm{h}}56^{\mathrm{m}}16.^{\mathrm{s}}90$, decl. $= -05^{\circ}50'43.''0$ (J2000) and its magnitudes are $V = 13.660$, $J = 12.377$, and $Ks = 11.974$ (Raiteri et al. 1998; Cutri et al. 2003). The photometric data have been corrected for the Galactic extinction with $A_V = 0.093$, $A_J = 0.026$, and $A_{Ks} = 0.010$. The measured optical and near-IR magnitudes by Kanata in the V, J, and Ks bands during the two year observations spanned $m_V = 15.54$–17.27 (56 data points), $m_J = 13.00$–14.58 (37 data points), and $m_{Ks} = 11.21$–11.47 (17 data points). Those data points are also shown in Figure 7.

We confirmed that the instrumental polarization was smaller than 0.1% in the V band using the observations of unpolarized standard stars. Hence, we did not apply any corrections for it. The zero point of the polarization angle is corrected as standard system (measured from north to east) by observing the polarized stars, HD19820 and HD25443 (Wolff et al. 1996). The polarization shows clear variability and the degree of

Table 2
List of Observatories that Contributed Data to the Campaign

Observatory	Detector/Telescope (diam.)	Band
	Gamma ray	
Fermi	LAT (survey mode)	>200 MeV
	X-ray	
Suzaku	XIS	0.5–10 keV
	HXD/PIN	15–50 keV
XMM-Newton	PN	0.5–10 keV
RXTE	PCA	3–10 keV
Swift	XRT	0.6–7 keV
	Ultraviolet, optical, infrared	
Swift	UVOT	$W2, M2, W1, U, B, V$
Spitzer	IRS	5–38 μm
	IRAC	3.6, 4.5, 5.8, 8.0 μm
	MIPS	24, 70, 160 μm
Abastumani, Georgia[a]	(70 cm)	R
Calar Alto[a,b]		R
Campo Imperatore, Italy[a]	AZT-24 (110 cm)	J, H, K
Crimean, Ukraine[a]	ST-7 (70 cm)	R
Goddard, USA[a]	GRT	R
Hiroshima, Japan	Kanata (150 cm)	V, J, Ks, polarization (V)
Kitt Peak, Arizona, USA[a]	MDM (130 cm)	R
La Silla, Chile	GROND (220 cm)	g, r, i, z, J, H, K
L'Ampolla[a]		R
Lowell (Perkins)[a]	Perkins	R
Lulin, Taiwan[a]	SLT (40 cm)	R
Roque, Canary Islands[a]	KVA (35 cm)	R, polarization (no filter)
Roque, Canary Islands[a]	LT (200 cm)	R, H
San Pedro Martir[a]	(84 cm)	R
St. Petersburg, Russia[a]	(40 cm)	R
Tijarafe[a]	(35 cm)	R
	Radio	
CARMA, USA	(array)	92.5, 227.5 GHz
Mauna Kea, USA[a]	SMA (8 × 6 m)	230, 345 GHz
Medicina, Italy[a]	(32 m)	5, 8, 22 GHz
Metsahovi, Finland[a]	(14 m)	37 GHz
Noto, Italy[a]	(32 m)	43 GHz
Owens Valley, USA	OVRO (40 m)	15 GHz
UMRAO, USA[a]	(26 m)	5, 8, 14.5 GHz

Notes.
[a] GASP-WEBT.
[b] Calar Alto data were acquired as part of the MAPCAT project: http://www.iaa.es/~iagudo/research/MAPCAT.

polarization was measured in the range of 3%–36% during our two year observational campaign. As we reported in Paper I, we found a rotation of the polarization angle by 208° together with a sharp drop of the degree of polarization from ~30% down to a few %. The event was coincident with a γ-ray flare (Periods D and E). In the second half of the two year observations, the source was generally in a quiet state in the optical band, and the degree of polarization was also relatively low.

3.8. Optical and Near-infrared: GROND

The Gamma-Ray burst Optical/Near-infrared Detector (GROND; Greiner et al. 2008) mounted at the MPI/ESO 2.2 m telescope at LaSilla observatory in Chile observed the field of 3C 279 in two nights of 2008 July (2008 July 30 and 2008 July 31) and four nights in 2009 January (2009 January 19 to 2009 January 22). In each observation, a total of 4 images in each $g'r'i'z'$ filter with integrations times of 35 s and 24 images of 10 s exposure in each JHK_s were obtained simultaneously.

GROND optical and near-IR data were reduced in standard manner using pyraf/IRAF (Tody 1993) similar to the procedure outlined in Krühler et al. (2008). The stacked images of each observation were flux calibrated against GROND observations of SDSS fields (Abazajian et al. 2009) taken immediately before or after the field of 3C 279 for the optical $g'r'i'z'$, and magnitudes of 2MASS field stars (Skrutskie et al. 2006) for the JHK_s filters. All data were corrected for the expected Galactic foreground reddening of $E_{(B-V)} = 0.029$ according to Schlegel et al. (1998). Results of GROND observations are summarized in Table 4.

Table 3
Results of GROND Observations

Filter	2008 Jul 31		2009 Jan 19–22		
	AB Magnitude	Flux (mJy)	AB Magnitude	Flux (mJy)	$A/A(V)$[a]
g'	17.62 ± 0.05	0.324 ± 0.015	16.06 ± 0.05	1.37 ± 0.06	1.23
r'	17.24 ± 0.05	0.462 ± 0.021	15.49 ± 0.05	2.31 ± 0.11	0.80
i'	16.83 ± 0.05	0.671 ± 0.031	15.05 ± 0.05	3.47 ± 0.16	0.62
z'	16.67 ± 0.05	0.776 ± 0.036	14.80 ± 0.05	4.37 ± 0.20	0.45
J	16.05 ± 0.06	1.387 ± 0.077	14.16 ± 0.06	7.86 ± 0.44	0.29
H	15.60 ± 0.07	2.098 ± 0.133	13.62 ± 0.07	12.90 ± 0.81	0.18
K	15.18 ± 0.09	3.062 ± 0.249	13.19 ± 0.09	19.18 ± 1.56	0.14

Notes. Results of both AB magnitude and flux are corrected for Galactic extinction. No significant daily variability was observed during the observations in 2009 January.
[a] Dereddening factors for correction of Galactic extinction.

Table 4
Spitzer Observation Log

Instrument	Start Time (UTC)	(MJD)	Duration (minute)	ObsID
MIPS	2008.7.31 11:09:06.3	54678.4647	9.19	27434240
	2009.2.15 07:08:08.6	54877.2973	14.61	27438592
	2009.2.16 23:12:32.0	54878.9670	14.61	27438080
	2009.2.17 20:42:36.5	54879.8629	14.61	27438848
	2009.2.18 19:39:30.8	54880.8191	14.60	27438336
	2009.2.19 14:19:04.4	54881.5966	14.60	27439360
	2009.2.20 09:23:37.4	54882.3914	14.60	27439104
IRS	2008.8.16 14:32:42.6	54694.6060	17.92	27425024
	2009.3.3 12:22:35.7	54893.5157	18.15	27435776
	2009.3.4 19:53:03.5	54894.8285	18.15	27437312
	2009.3.6 10:50:02.7	54896.4514	18.16	27436544
	2009.3.7 00:46:03.4	54897.0320	18.16	27435520
	2009.3.8 12:08:53.5	54898.5062	18.18	27437056
	2009.3.9 18:39:51.2	54899.7777	18.18	27436288
IRAC	2008.8.17 06:57:26.3	54695.2899	10.64	27429632
	2009.3.10 19:26:05.5	54900.8097	10.69	27433216
	2009.3.11 22:05:54.7	54901.9208	10.70	27432448
	2009.3.13 05:13:56.9	54903.2180	10.71	27433728
	2009.3.14 04:12:41.8	54904.1755	10.72	27432960
	2009.3.15 03:04:16.9	54905.1280	10.73	27433984
	2009.3.16 14:58:46.6	54906.6241	10.75	27433472

3.9. Infrared: Spitzer

We observed 3C 279 with *Spitzer* Infrared Spectrograph (IRS), Multiband Imaging Photometer for *Spitzer* (MIPS), and Infrared Array Camera (IRAC) at several epochs in 2008 and 2009 under the *Spitzer* program PID50231 (PI: A. Wehrle; see Table 3). The observations were conducted once with each instrument in 2008 July and August and approximately daily

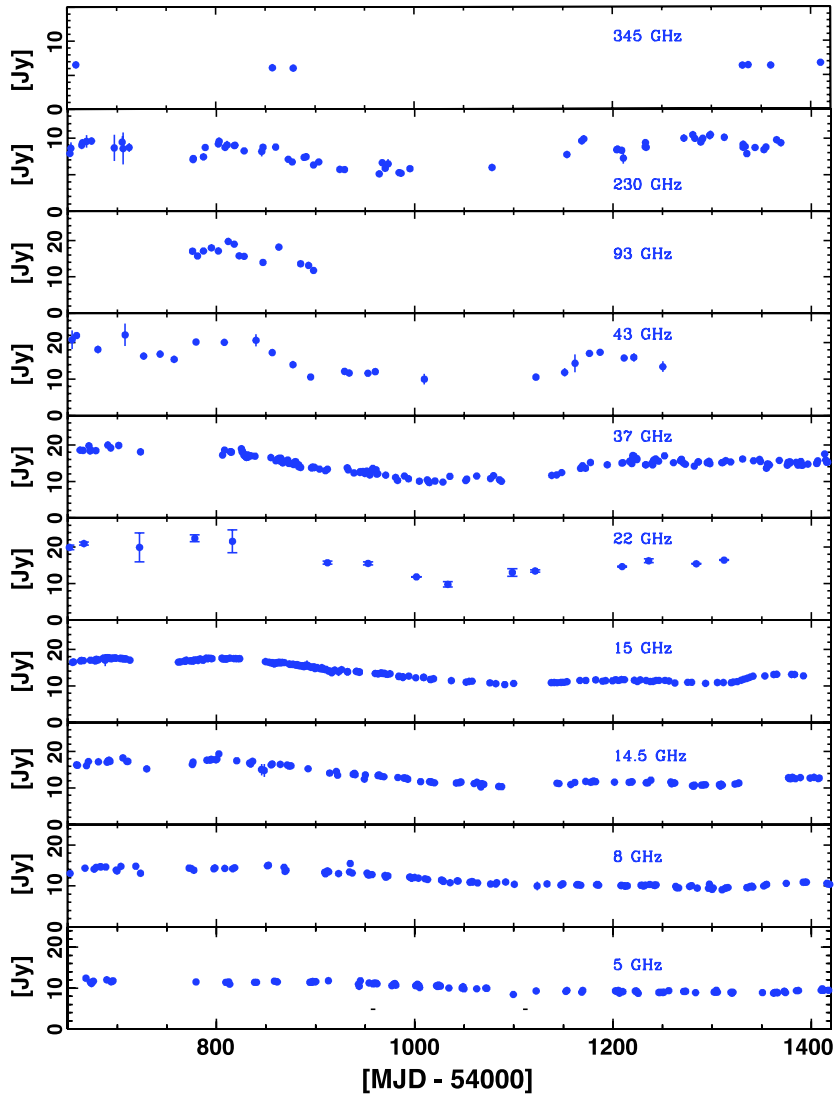

Figure 8. Radio light curves of 3C 279 from 2008 August to 2010 August measured at all observed radio frequencies: 345 GHz (SMA), 230 GHz (CARMA, SMA), 93 GHz (CARMA), 43 GHz (Noto), 37 GHz (Metsahovi), 22 GHz (Medicina), 15 GHz (OVRO), 14.5 GHz (UMRAO), 8 GHz (Medicina, UMRAO), and 5 GHz (Medicina, UMRAO).

(A color version of this figure is available in the online journal.)

during the instrument campaigns in the 2009 February–March visibility window.

For the IRS observations, high-accuracy blue peakup observations on a nearby star were used to center the spectrograph slit on the target. 3C 279 was observed with the low-resolution SL2, SL1, LL2, and LL1 modules, for three cycles of 14 s at each of two nod positions. *Spitzer*-IRS data reductions began with S18.7 *Spitzer* Science Center pipeline-processed, background-subtracted data. The background was removed by subtracting the alternate nod for each pointing. Additional processing steps were applied to clean bad data, remove fringes, and match and trim spectral orders. First, we cleaned bad, rogue pixels using the *Spitzer* Science Center procedure IRSCLEAN V2.0. One-dimensional spectra were then extracted using the standard point-source aperture and flux calibration in SPICE ver. 2.3. We used a custom spectral defringing tool to remove fringes introduced by the pointing-dependent instrumental flat field. This tool uses a predetermined flat-field fringing correction function, which is shifted to match and remove the observed fringes in the spectrum. Spectral orders were trimmed, and the SL2 and SL1 orders were scaled up by a factor of 1.06 to empirically correct for pointing-dependent point-source slit losses. Finally, the nod-spectra were averaged and combined into a single spectrum covering 5.2–35 μm rest wavelength. Figure 9 shows the reduced IRS spectra in the νF_ν representation.

We used the pipeline MIPS images (ver. 18) for aperture photometry using 13″, 35″, and 50″ radius for 24, 70, and 160 μm bands, respectively, with aperture corrections from Tables 3.13, 3.14, and 3.16 of the MIPS Data Handbook (ver. 3.2). No 160 μm data were obtained in 2008 August because the array was not cooled during that campaign. 3C 279 has very low ecliptic latitude (0.°2), hence the observed transients can be attributed to passing asteroids which appeared in various MIPS images. We used 6″ radius apertures for IRAC photometry on the pipeline data (ver. 18) with aperture corrections tabulated in Table 5.7 of the IRAC Data Handbook (ver. 3.0).

The *Spitzer*-MIPS photometric repeatability and absolute calibration uncertainties at 24 μm are, respectively, 0.4% and 4%; at 70 μm, 4.5% and 5%; and at 160 μm, 5% and 12% (Engelbracht et al. 2007; Gordon et al. 2007; Stansberry et al. 2007). We therefore adopt overall uncertainties of 10%, 10%, and 20% at 24, 70, and 160 μm, respectively. No color correction

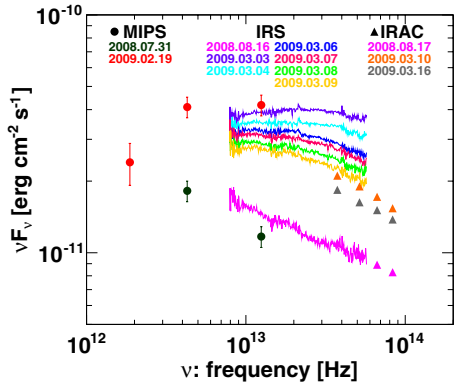

Figure 9. Spectral energy distribution of 3C 279 in the infrared band measured by *Spitzer*-IRS. IRS spectra from highest to lowest are on 2009 March 3, 2009 March 4, 2009 March 5, 2009 March 6, 2009 March 7, 2009 March 9, and 2008 August 16. Representative flux data points measured by *Spitzer*-MIPS (circles) and *Spitzer*-IRAC (triangles) are also included.

(A color version of this figure is available in the online journal.)

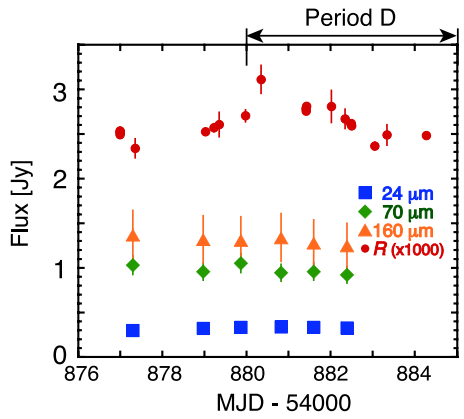

Figure 10. Light curve of 3C 279 at 24 μm, 70 μm, and 160 μm measured by *Spitzer*-MIPS. The error bars correspond to 10%, 10%, and 20%, respectively, for each band as mentioned in the text in Section 3.9. Optical *R*-band data taken by the ground-based telescopes are also plotted in red color for comparison.

(A color version of this figure is available in the online journal.)

has been applied to the data because the slope and smoothness of the spectrum over the bandpasses are not known. Figure 10 describes the MIPS flux history during the six epochs from 2009 February 15 to 20 together with *R*-band flux for comparison. No significant flux variation is found in all MIPS bands during those epochs, which include period D.

The *Spitzer*-IRAC calibration uncertainty is 3% overall and has photometric repeatability of 1.5% (Reach et al. 2005). We adopt the overall IRAC calibration uncertainty of 3%, but note the following characteristics of our images. In our IRAC frames, two standard comparison stars used in blazar monitoring were visible in the 3.6 μm images (Star 1 and Star 2).[60] One comparison star, Star 2, was visible in the 4.5, 5.8, and 8 μm images, located at the interstice of the chopping regions where the data are noisier than elsewhere. The spacecraft orientation, and hence the chopping orientation, was 180° different between 2008 July–August and 2009 March. The standard deviations in comparison Star 2's measurements in 2009 March at 3.6, 4.5, 5.8, and 8 μm are 0.68 mJy, 0.08 mJy, 0.08 mJy, and 0.09 mJy (5%, 1%, 2%, and 3%), respectively. The high 3.6 μm standard deviation was affected by a single high value on 2009 March 11, for which we found no obvious cause; excluding that value resulted in a standard deviation of 0.06 mJy (0.5%). In contrast, the flux of 3C 279 shows a steady decrease of 10%, 12%, 14%, and 13% at 3.6, 4.5, 5.8, and 8.0 μm, respectively, during the six epochs from 2009 March 10–16 as shown in Figure 11.

[60] See http://www.lsw.uni-heidelberg.de/projects/extragalactic/charts/1253-055.html (Raiteri et al. 1998; Villata et al. 1997).

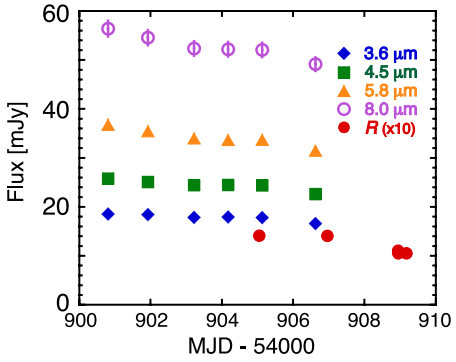

Figure 11. Light curve of 3C 279 at 3.6 μm, 4.5 μm, 5.8 μm, and 8.0 μm measured by *Spitzer*-IRAC. The error bars correspond to 3% for all IRAC bands as mentioned in the text in Section 3.9. Optical *R*-band data taken by the ground-based telescopes are also plotted in red color for comparison.

(A color version of this figure is available in the online journal.)

3.10. Radio: CARMA

Observations were obtained at mean frequencies of 92.5 and 227.5 GHz using the Combined Array for Research in Millimeter-wave Astronomy (CARMA; Bock et al. 2006). In all cases, the nominal signal to noise ratio exceeded 400 and calibration uncertainties dominated the errors. The source is bright enough to permit self-calibration on timescales of less than a minute and so atmospheric decorrelation was not expected to affect our results significantly even at the long baselines. However, observations in poor weather were not used due to the difficulty of reliably measuring pointing offsets in these conditions.

Data calibration and analysis was done with the MIRIAD software package (Sault et al. 1995). Flux densities were determined by first using phase self calibration with a short enough averaging interval to avoid any atmospheric phase decorrelation, then the flux density was determined from the vector average fringe amplitude at the position of 3C 279 over all baselines. For a strong point source such as 3C 279 this provides very robust and unbiased amplitude estimate independent of the weather or the interferometer baselines. We rely on regular system temperature measurements to provide flux calibration relative to the fixed system sensitivity. The absolute flux calibration of CARMA observations is usually quoted as 10%–15%. However, based on measurements made on the blazar 3C 454.3 we estimated the relative flux calibration at each frequency to be within 5% at 3 mm and 10% at 1 mm. The radio fluxes at 92.5 and 227.5 GHz measured by CARMA correspond to $F_{92.5\,\mathrm{GHz}} = 11.7$–$19.7$ Jy (14 data points) and $F_{227.5\,\mathrm{GHz}} = 6.3$–$9.2$ Jy (14 data points). Figure 8 includes the flux history of those radio data.

3.11. Radio: OVRO 40 m

The Owens Valley Radio Observatory (OVRO) 40 m radio data were collected as part of an ongoing long-term, fast-cadence γ-ray blazar monitoring campaign, described in detail in Richards et al. (2011). Flux densities were measured in a 3 GHz bandwidth centered on 15.0 GHz using dual, off-axis 2.′5 FWHM beams with 12.′95 separation. Dicke switching against a blank sky reference field to remove gain fluctuations

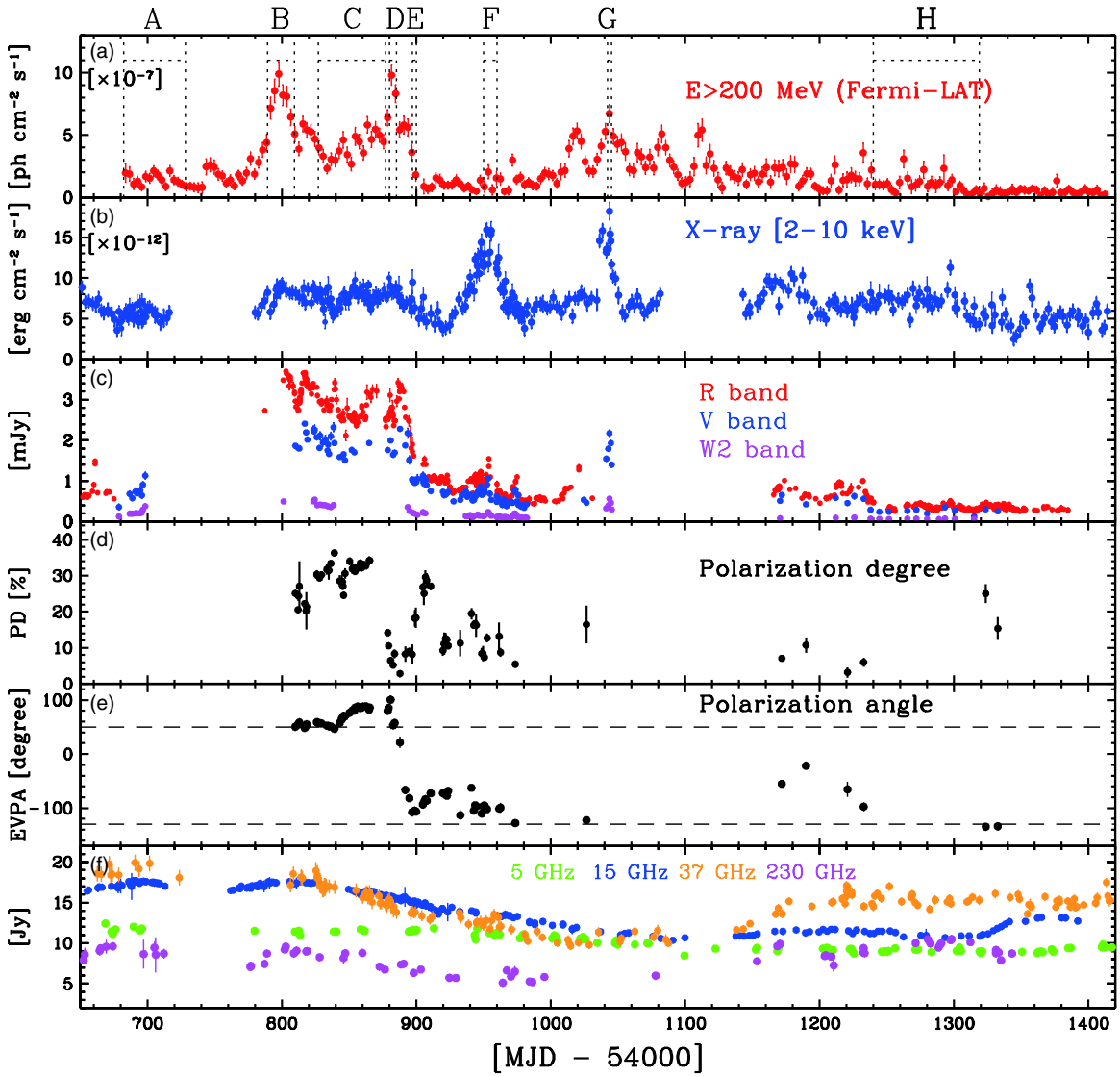

Figure 12. Multi-band light curves of 3C 279 for two years from 2008 August to 2010 August. (a) Gamma-ray flux above 200 MeV averaged over three days. (b) X-ray flux between 2 and 10 keV measured by *Swift*-XRT and *RXTE*-PCA. (c) UV–optical fluxes in *R* band (red), *V* band (blue), and *W*2 band (magenta). (d) Polarization degree in the optical band. (e) Polarization angle in the optical band. The horizontal dashed lines refer to the angle of 50° and −130°. (e) Radio fluxes in 230 GHz band (magenta), 37 GHz band (orange), 15 GHz band (blue), and 5 GHz band (green). All X-ray, UV, and optical data are corrected for the Galactic absorption.
(A color version of this figure is available in the online journal.)

and atmospheric and ground contamination were used. Flux densities from this program are found to have a minimum uncertainty of 4 mJy (mostly thermal) and a typical uncertainty of 3% for brighter sources. During the period included here, 3C 279 was observed as a pointing calibrator. The flux density scale was referred to the value for 3C 286 (3.44 Jy at 15 GHz; Baars et al. 1977) with a scale uncertainty of about 5%. The radio flux at 15 GHz measured by OVRO was ranging from 11.1 to 18.0 Jy among 124 data points during the two year observations. The light curve of the OVRO radio data is also plotted in Figure 8.

4. RESULTS OF THE MULTI-WAVELENGTH OBSERVATIONS

4.1. Correlations of Light Curves in Various Bands

The multi-band light curves of 3C 279 are presented in Figure 12. They include (a) γ-ray flux above 200 MeV (*Fermi*-LAT), (b) 2–10 keV X-ray flux measured by *Swift*-XRT and *RXTE*-PCA, (c) optical-UV fluxes in *R* band (GASP), *V* band (*Swift*-UVOT and Kanata), and *W*2 band (*Swift*-UVOT), (d,e) degree and angle of optical polarization (Kanata and KVA), and (f) radio fluxes in the 230, 37, 15, and 5 GHz bands (GASP, CARMA, and OVRO). We note that the X-ray fluxes determined by *Suzaku* and *XMM-Newton* are entirely consistent with those plotted in Figure 12. The extensive data set obtained in many bands for 3C 279 allows us to make general statements regarding the relative flux variability in various spectral bands, and the relationship of the time series to each other. The first such feature of the multi-band light curves is a general—although not exact—trend where the IR through optical emission seems to be correlated with the γ-ray flux. We calculated the discrete correlation function (DCF; Edelson & Krolik 1988) to quantify the correlation of the flux variations between the γ-ray and other bands, and to determine whether we can measure any clear lag between the bands.

For the DCF calculations, we use the γ-ray fluxes averaged over an interval of 1 day as shown in the top panel of Figure 1.

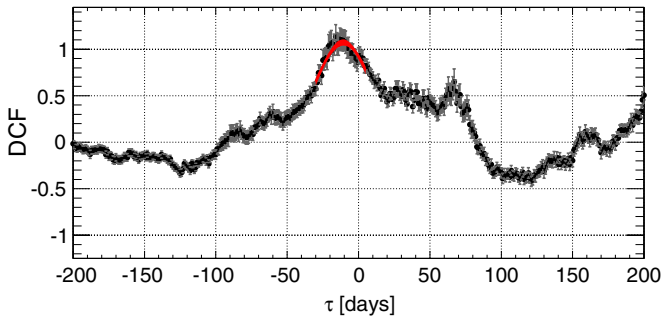

Figure 13. Discrete correlation function (DCF) derived for the γ-ray and optical R bands. Positive values of "τ" correspond to flux variations in the γ-ray band lagging flux variation in the optical band. The red curve represents a Gaussian fit to the data between -30 and 5 days. See the text for the fitting results.

(A color version of this figure is available in the online journal.)

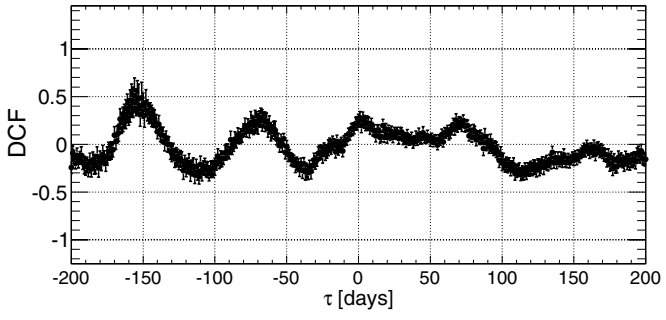

Figure 14. DCF between derived for the γ-ray and X-ray bands. Positive values of "τ" correspond to flux variations in the γ-ray band lagging flux variation in the X-ray band.

The resulting DCF between γ-ray and optical R-band fluxes is shown in Figure 13. Positive values of "τ" correspond to flux variations in the γ-ray band lagging flux variations in the other bands. In the DCF between γ-ray and optical R-band fluxes, a peak can be seen close to zero lag. We fit the DCF data points in the range between -30 and 5 days using a Gaussian function of the form $\mathrm{DCF}(\tau) = C_{\max} \times \exp[(\tau - \tau_0)^2/\sigma^2]$, where $C_{\max}$ is the peak value of the DCF, τ_0 is the time at which the DCF peaks, and σ is the Gaussian width of the DCF. The fit yields a position of the peak at $\tau_0 = -10.7 \pm 0.7$ days, corresponding to a value of $C_{\max} = 1.07 \pm 0.03$ with a dispersion of $\sigma = 19.4 \pm 1.4$ days. The result implies that the optical emission is possibly delayed with respect to the γ-ray emission by about 10 days.

In the framework of the one-zone synchrotron + external-radiation Compton (ERC) models, the same electron population, of roughly the same energies, is responsible for the radiation in both the optical and γ-ray bands. There, the observed lag can result from different profiles of the decreasing magnetic and radiation energy densities along the jet: we show that idea quantitatively in the Appendix. As is shown there, a very steep drop of the external radiation energy density is required to explain the lag in a conical jet with magnetic field $B' \propto 1/r$, where r is the distance along the jet. This condition can be relaxed in the scenario involving the re-confinement of a jet (e.g., Daly & Marscher 1988; Komissarov & Falle 1997; Nalewajko & Sikora 2009). In such a case, the magnetic field intensity can drop more slowly than $1/r$. If the lag of the optical emission is confirmed, the application of the results in the Appendix to the $\sim$10 day lag may imply the location of the active "blazar zone" at distances of a few pc in agreement with those postulated to explain the optical polarization swing (Periods D and E) in terms of a region containing an enhanced density of ultra-relativistic electrons propagating along a curved trajectory (Paper I). It is worth noting that similar γ-ray/optical lags have been reported during the outbursts of 3C 279 in early 1999 Hartman et al. (2001b), of PKS 1502+106 in 2008 (Abdo et al. 2010d), of PKS 1510−089 in early 2009 (Abdo et al. 2010a; D'Ammando et al. 2011), and of AO 0235+164 in late 2008 (Agudo et al. 2011b; Ackermann et al. 2012). On the other hand, no significant lags between γ-ray and optical signals have been detected in 3C 454.3 in late 2008 (Bonning et al. 2009; Jorstad et al. 2010), in 3C 66A in 2008 October (Abdo et al. 2011), and in OJ 287 in 2009 October (Agudo et al. 2011a). Based on investigations of long-term light curves of 3C 454.3 during 2008–2010, Raiteri et al. (2011) have shown that the optical and γ-ray flux variations are not always simultaneous and have proposed a geometrical scenario to explain the change in the γ/optical flux ratio during the outburst peaks in 3C 454.3. It is expected that the on-going multi-band monitoring of blazars will enable us to quantify such lags and find out how common they are.

Different behavior is apparent in the radio flux, where the energies of radio-emitting electrons are very different from the energies of the electrons involved in producing the observed optical and γ-ray emission. Variability appears to be much less rapid, and the excess variance (F_{var}; see definition in Equation (1)) in the radio regime is quite modest; for instance, 0.145 ± 0.004 at 37 GHz, 0.165 ± 0.001 at 15 GHz, and 0.104 ± 0.001 at 5 GHz. Those values are significantly less than ones in the γ-ray or optical bands. This suggests that the synchrotron emission from the γ-ray emitting region is self-absorbed at these wavelengths. The observed radiation is produced at much larger distances, where the light-travel effects smear out the sharp, rapid variability patterns observed in the optical and γ-ray bands.

Perhaps the most surprising behavior—and difficult to explain in the context of simple, one-component, single-zone models—is the relationship of the X-ray light curve to those in the IR–optical or γ-ray bands. In Paper I, we reported that the X-ray time series exhibits a relatively rapid, symmetrical flare at $\sim$ MJD 54950 (Period F) with a duration of $\sim$20 days, which is *not* accompanied with any prominent IR/optical or γ-ray flares. As we argued in Paper I, the hard (rising in νF_ν representation) X-ray spectrum is unlikely to be the "tail" of the synchrotron emission, but instead, it is more likely to be produced by the low-energy end of the electron distribution radiating via inverse-Compton process.

The continuing monitoring of the object in the X-ray band revealed another X-ray flare at $\sim$MJD 55040 (Period G), $\sim$90 days after the first X-ray flare. The separation of the two X-ray flares is remarkably close to the temporal separation of the two γ-ray flares, with the two pairs delayed with respect to each other by $\sim$155 days. Figure 14 presents the calculated DCF between γ-ray and X-ray fluxes, which shows a modest peak at ~ -155 days with a correlation coefficient of 0.6–0.7 and indicates no correlation between the γ-ray and the X-ray bands with zero lag. While confirming the physical connection of the two pairs would be very important, we cannot currently envision any situation where the two would be causally connected; the 155 day lag would imply the distance of the X-ray flare production $\sim 155\Gamma_{\mathrm{j}}^2$ lt-day $\sim 50(\Gamma_{\mathrm{j}}/20)^2$ pc and at such a distance should be accompanied by radio flares, which are not seen in our data. In such a scenario, the X-ray flares should be significantly broadened compared to the γ-ray flares; however, we observe a similar temporal structure in both bands.

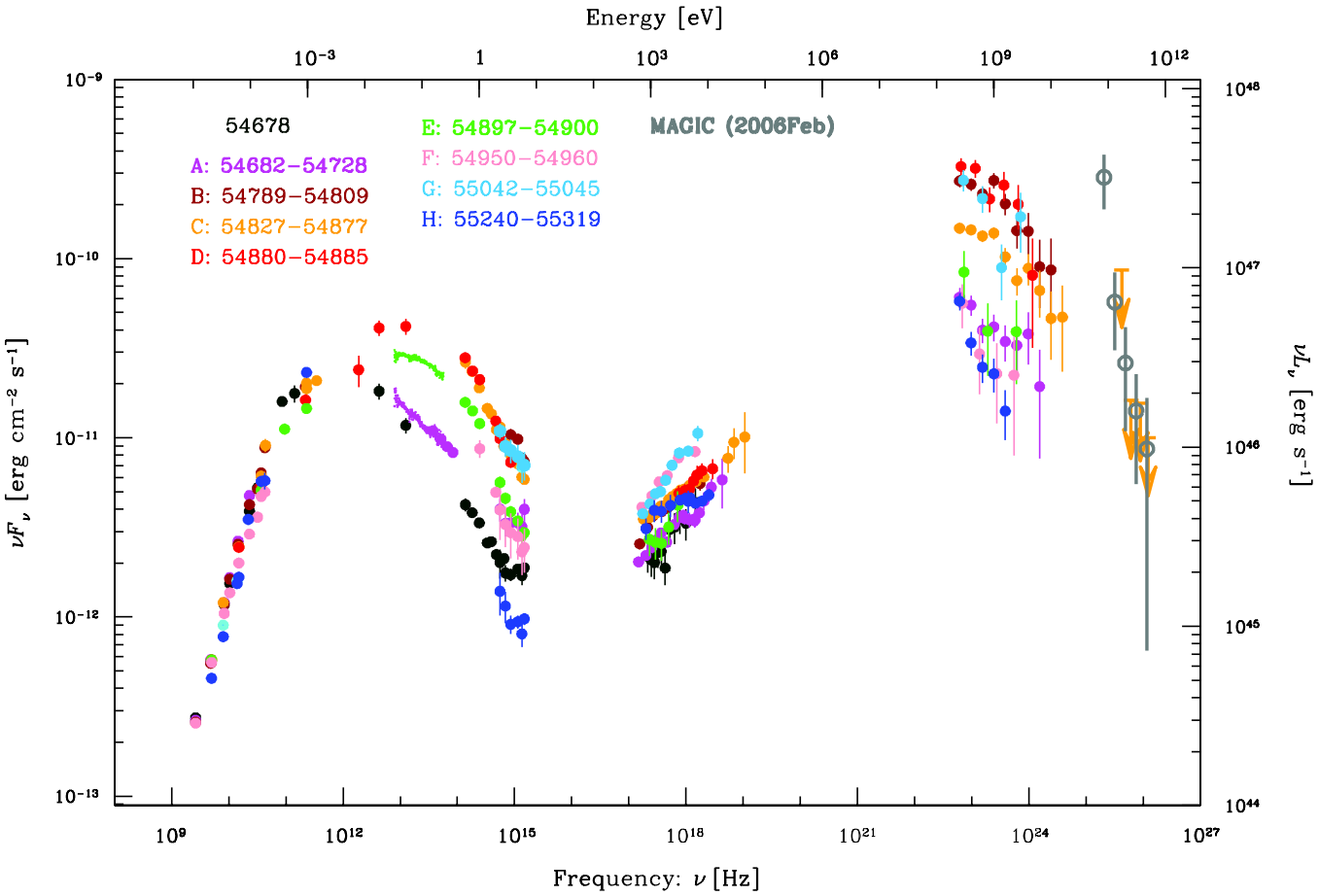

Figure 15. Time-resolved broadband spectral energy distributions of 3C 279 measured in Periods A–H (as defined in Table 1) and on 2008 July 31 (MJD 54678), covered by our observational campaigns in 2008–2010. X-ray, UV–optical–near-IR data are corrected for the Galactic absorption. Five-digit numbers in the panel indicate MJD of the periods. For comparison, the gray open circles in the very high energy γ-ray band represent measured spectral points by MAGIC in 2006 February (Albert et al. 2008).

Furthermore, we note that there are some optical and γ-ray peaks that might well be associated with the second X-ray flare. Hence, it is possible that the two prominent γ-ray/optical flares (Periods B and D), together with the subsequent two X-ray flares (Periods F and G), form a sequence of four events separated by a similar time intervals. Those intervals, in turn, can be possibly determined by instabilities in the jet launching region. Here, the different broadband spectra during these events may result from small changes of parameters, such as the jet direction, Lorentz factor, and/or location and geometry of the dissipation event.

A weak (and sporadically almost absent) correlation between X-rays and other spectral bands can also result from such processes that preferably contribute to radiation in the X-ray band. They can be related to the following three mechanisms/scenarios.

1. *Bulk-Compton process*. This involves Compton-scattering of ambient optical/UV light by the *cold* (non-relativistic) electrons in the jet. This mechanism is most efficient close to the accreting black hole where the processes responsible for the variability of X-rays may operate independently of those at larger distances and producing there variable non-thermal radiation (Begelman & Sikora 1987). A drawback of this scenario can be that the bulk-Compton spectrum is predicted to have a similar shape as the spectrum of the external radiation field (Ackermann et al. 2012), which significantly differs from what we observe in the X-ray band.
2. *Inefficient electron acceleration*. Acceleration of the relativistic electrons at proton-mediated shocks is likely to proceed in two steps: in the first one low-energy electrons may be pre-accelerated via, for example, some collective processes involving protons; in the second step, they may participate in the first-order Fermi acceleration process. If under some conditions the electron–proton coupling is inefficient, the fraction of electrons reaching the Fermi phase of acceleration will be small. In this case the X-rays, originating from lower energy electrons, are produced efficiently, while the γ-rays and optical radiation that involve more relativistic electrons are not.
3. The X-rays can be also contributed by hadronic processes, specifically by the pair cascades powered by protons losing their energy in the photo-mesonic process (Mannheim & Biermann 1992). For this process to be efficient, it requires extreme conditions (Sikora et al. 2009; Sikora 2011); however, operating in the very compact central region, at distances less than few hundred gravitational radii, it may occasionally dominate in the X-ray band.

4.2. Broadband Spectral Energy Distribution

Figures 15 and 16 show broadband SEDs of 3C 279 in all periods as defined in Table 1. In addition, we also extracted an SED using data taken on 2008 July 31 (MJD 54678), which has a good energy coverage of the synchrotron emission component

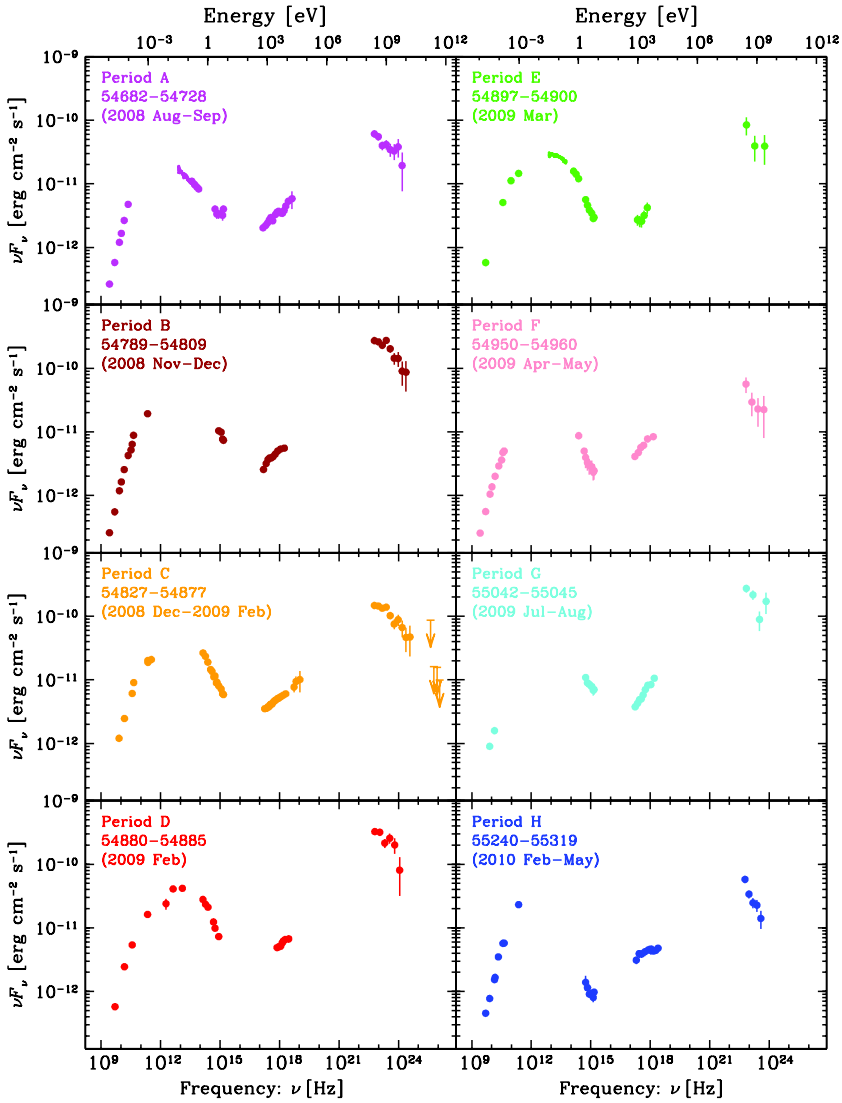

Figure 16. Time-resolved broadband spectral energy distributions of 3C 279 in each period (A–H), covered by the campaigns. The data points are the same as ones in Figure 15, but are plotted in a separate panel for each period. Five-digit numbers in each panel indicate MJD of the observing period of each broadband spectrum.
(A color version of this figure is available in the online journal.)

including *Spitzer* and GROND data, although the γ-ray data by *Fermi*-LAT are not available at that time because this was before the beginning of normal, all-sky science observations with *Fermi*-LAT. Both SEDs for Period D (2009 February; corresponding to the brightest γ-ray flare coincident with the optical polarization swing) and Period F (2009 April; corresponding to the first isolated X-ray flare) have already been partially reported in Figure 2 of Paper I. New *Spitzer*-MIPS data points are included in the SED for Period D in this paper. In Period C, there are observations by MAGIC, which provide upper limits above 100 GeV (Aleksić et al. 2011). For comparison, we also include VHE γ-ray fluxes detected with the MAGIC telescope in 2006 February as gray points (Albert et al. 2008) in Figure 15.

This is the richest set of time-resolved spectra ever collected for this source. The spectral coverage of the synchrotron bump is unprecedented, allowing us not only to constrain the parameters of the emission models, but also to study their time evolution. As we discussed in Section 2.4, the shape of the γ-ray spectrum deviates from a simple power law, in similarity to other FSRQ blazars. Strong variability, over one order of magnitude, is evident in near-IR/optical/UV and γ-ray bands. This contrasts with the moderate variability in the radio/mm and X-ray bands.

Particularly interesting is the behavior of this source in the mid-IR band, around $\sim 10^{13}$ Hz, where significant spectral variability is observed. In the low state in Period A, the mid-IR spectrum is relatively soft and can be extended with a power-law shape to the optical/UV band. In this case, the synchrotron component peaks in the mm/sub-mm band ($\sim 10^{11}$–10^{12} Hz). However, in the high state in Periods D and E, the mid-IR spectrum is much harder and shows a significant curvature. In Period D, there is a clear spectral break at $\sim 3 \times 10^{12}$ Hz ($\sim 100\,\mu$m). The spectral index between the $70\,\mu$m ($\sim 4.3 \times 10^{12}$ Hz) and $160\,\mu$m ($\sim 1.9 \times 10^{12}$ Hz) points is $\alpha_{70-160} = 0.35 \pm 0.23$, taking into account systematic errors described in Section 3.9. The synchrotron peak is located in the mid-IR band, at a frequency one order of magnitude higher than in the low state. This indicates that there are two independent synchrotron bumps, possibly produced at different locations. The mid-IR-peaking component, seen only in the IR/optical/UV flaring state, is characterized by a strong and rapid variability. The mm/sub-mm peaking component is more

persistent and dominates when the source is in the low state. The complex shape of the SED between the mm band and the 70 μm point in Period D requires a coexistence of these two components. A similar scenario of multiple synchrotron components was investigated in the case of 3C 454.3 by Ogle et al. (2011).

In the X-ray band, despite the smaller variability amplitude, we observe some spectral changes. In particular, in Periods F and G, which represent the two isolated X-ray flares, the spectrum is very similar and harder than on average. Figure 15 shows that these flares are not energetically important. If we extrapolate the X-ray spectra with power laws to the γ-ray band, we underpredict the observed γ-ray flux in Periods B, C, D, and H. Periods B, C, and D coincide with the high-activity γ-ray state. This indicates that the X-ray flux cannot originate from the same emission component as the γ-ray flux, at least in the flaring state. Because the γ-rays are correlated with the optical flux but not with the X-ray flux, the γ-rays can be related to the mid-IR-peaking synchrotron bump while the X-rays may correspond to the mm/sub-mm peaking synchrotron bump. We explore this possibility when modeling the SEDs at Periods A and D in Section 5.2.

5. MODELING THE BROADBAND EMISSION

We have fitted selected SEDs with one-zone leptonic models described in Moderski et al. (2003), including synchrotron emission and self-absorption, Comptonization of the local synchrotron radiation (SSC component) and external photons (ERC component), but also including the opacity due to internal pair-production. The external radiation includes broad emission lines (BEL) and infrared dust emission (IR). Their energy densities in the jet comoving frame as functions of the distance r along the jet are approximated by the formulae:

$$u'_{\rm BEL}(r) = \frac{\xi_{\rm BEL}\Gamma_{\rm j}^2 L_{\rm D}}{3\pi r_{\rm BEL}^2 c[1+(r/r_{\rm BEL})^{\beta_{\rm BEL}}]} \quad (2)$$

$$u'_{\rm IR}(r) = \frac{\xi_{\rm IR}\Gamma_{\rm j}^2 L_{\rm D}}{3\pi r_{\rm IR}^2 c[1+(r/r_{\rm IR})^{\beta_{\rm IR}}]}, \quad (3)$$

where $\xi_{\rm BEL} = 0.1$ and $\xi_{\rm IR} = 0.1$ are the fractions of the disk luminosity $L_{\rm D} \simeq 2\times10^{45}$ erg s^{-1} reprocessed into emission lines and into hot dust radiation, respectively, $r_{\rm BEL} = 0.1(L_{D,46})^{1/2}$ pc and $r_{\rm IR} = 2.5(L_{\rm D,46})^{1/2}$ pc [$L_{\rm D,46} \equiv L_{\rm D}/10^{46}$] are the characteristic distances where such reprocessing takes place, and $\Gamma_{\rm j}$ is the jet Lorentz factor. The external radiation fields are approximated in the jet comoving frame by Maxwellian spectra peaked at photon energies $E'_{\rm BEL} \sim 10$ eV $\times\,\Gamma_{\rm j}$ and $E'_{\rm IR} \sim 0.3$ eV $\times\,\Gamma_{\rm j}$. While the radiation density profile in the frame external to the jet should satisfy $\beta_{\rm BEL(IR)} \leqslant 2$, it is not applied to the profile in the jet comoving frame. This is because the transformation of radiation density depends on the angular distribution of external radiation, with radiation arriving at small incidence angles to the jet velocity vector being actually deboosted. This can result in a steeper profile of the radiation density in the jet comoving frame. Here, we adopt $\beta_{\rm BEL} = 3$ (Sikora et al. 2009) and $\beta_{\rm IR} = 4$ (see Section 5.1). We assume a conical jet geometry; the magnetic field, assumed to be dominated by the toroidal component, is taken to decline with distance r as $B' \propto 1/r$. Electrons are injected with a double-broken power-law distribution $Q(\gamma) \propto \gamma^{-p}$ with $p = p_1$ for $\gamma < \gamma_{\rm br1}$, $p = p_2$ for $\gamma_{\rm br1} < \gamma < \gamma_{\rm br2}$, and $p = p_3$ for $\gamma > \gamma_{\rm br2}$. Their evolution, including injection at a constant rate as well as radiative and adiabatic cooling, is followed over a distance $\Delta r = r/2$, where r is the position at which the injection ends. The emission is integrated over spherical thin shells within a conical region of opening angle $\theta_{\rm j} = 1/\Gamma_{\rm j}$. The observer is located within the jet opening cone, i.e., $\theta_{\rm obs} \lesssim \theta_{\rm j}$.

We begin by modeling the SED in Period D, which is the highest γ-ray state reached by the source during our observational campaigns. In Paper I, we showed that the flare event was accompanied by an optical polarization swing and proposed two interpretations of this event. The first one involved a cloud containing ultra-relativistic particles propagating along a curved trajectory. The duration of the polarization swing constrains the location of the cloud to be at a few parsecs from the central supermassive black hole, in the region where external radiation is dominated by the infrared dust emission. In Section 5.1, we present an ERC-IR model describing the SED in Period D and a physically related model of the SED in Period E. The second interpretation of the polarization swing involved the jet precession, which allowed arbitrary location of the emitting region, including the broad-line region. In Section 5.2, we present an ERC-BEL model of the SED in Period D. We show that in this scenario the far-IR break arises due to synchrotron self-absorption. We also show an ERC-IR model of the SED in Period A, which can explain the mm/far-IR and X-ray emission, as well as the low-state optical and γ-ray flux levels.

We assume the scenario where the X-ray emission is unrelated to the flaring component, since it showed little variability during the correlated γ-ray/optical flares. Our one-zone models of the flaring states are fitted only to the IR/optical/UV and γ-ray data, treating the simultaneous X-ray spectrum as only an upper limit to the SSC component and the ERC component from the low-energy electrons. The large γ-ray/X-ray luminosity ratio forces us to adopt a very hard electron energy distribution at low energies ($p = 1$), which can be alternatively obtained by imposing a minimum electron Lorentz factor $\gamma_{\rm min} \gg 1$.

5.1. Propagation Scenario for the Emitting Region

An intrinsically spherically symmetric emitting region is expected to produce the observed electric polarization vector aligned with the projected velocity of the emitting region. Nalewajko (2010) presented a simple model of its trajectory to explain the event of simultaneous smooth variations of the polarization degree and angle during the polarization swing which has been reported in Paper I. This model adopts a constant jet Lorentz factor $\Gamma_{\rm j} = 15$ and can be used to predict the viewing angles for a given observation time. For Period D we estimate $\theta_{\rm obs,D} \sim 1.^\circ5$, while for Period E: $\theta_{\rm obs,E} \sim 2.^\circ4$. Between Periods D and E ($\Delta t \sim 15$ days), the emitting region propagates over a distance $\Delta r \sim \Gamma_{\rm j}^2 c(\Delta t) \sim 2.8$ pc.

In Figure 17 we show Model D1 fitted to the SED in Period D at $r = r_{\rm IR}$ and Model E1 fitted to the SED in Period E at $r = r_{\rm IR} + \Delta r$. Model parameters are listed in Table 5. Both models use the magnetic field scaled to the same value at the distance of 1 pc. In order to explain the difference in the luminosity ratio of the ERC component and the synchrotron component, which decreased by factor ~4 between Model D1 and Model E1, we assume a distribution of the comoving IR radiation energy density dropping steeply with distance, adopting $\beta_{\rm IR} \sim 4$. This corresponds to a strongly stratified torus structure, with a significant concentration of hot dust very close to the sublimation radius (see, e.g., Mor & Netzer 2012). We should note that, although the relatively soft γ-ray spectrum was

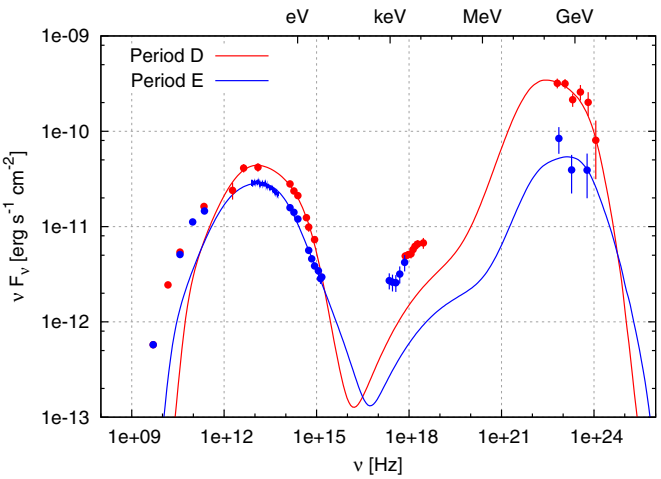

Figure 17. Emission models D1 (red line) and E1 (blue line) fitted to the spectral states at Periods D and E, respectively. Periods D and E correspond to the first five days and the last three days of the γ-ray flaring event accompanied by an optical polarization change, respectively. Those models adopt our "propagation scenario," where external radiation is dominated by infrared dust emission. We assume that the X-ray emission is not related to the flaring component, and consider the X-ray fluxes as only upper limits to the SSC and the ERC components during the flaring event. See the text in Sections 5 and 5.1 for details of the models and Table 5 for model parameters.

(A color version of this figure is available in the online journal.)

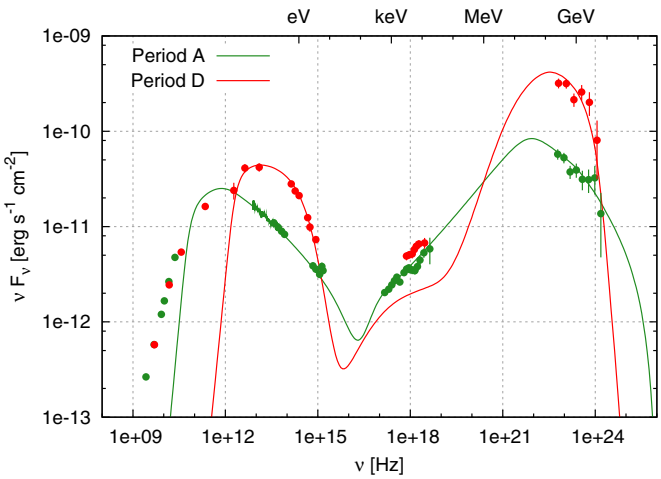

Figure 18. Emission Models A2 (green line) and D2 (red line) fitted to the spectral states at Periods A and D, respectively. Period A represents a quiescent state, and Period D corresponds to the γ-ray flaring event accompanied by an optical polarization change. Those models adopt our "jet precession scenario," which assumes the γ-ray flaring event (Period D) occurs within the broad-line region while the low-steady emission component (Period A) is generated outside the broad-line region. See the text in Sections 5 and 5.2 for details of the models and Table 5 for model parameters.

(A color version of this figure is available in the online journal.)

Table 5
Parameters of Emission Models

Model	D1	E1	D2	A2
Ext. rad.[a]	IR	IR	BEL	IR
r (pc)	1.1	3.9	0.045	3.9
R (pc)[b]	0.07	0.26	0.0023	0.19
Γ_j	15	15	20	20
θ_j [(°)]	3.8	3.8	2.9	2.9
θ_{obs} (°)	1.5	2.4	1.7	1.7
$B'_{1\,pc}$ (G)[c]	0.14	0.14	0.15	0.15
u'_{ext} (10^{-4} erg cm^{-3})[d]	78	0.97	8×10^4	1.8
γ_{br1}	800	800	170	440
γ_{br2}	6500	5000	1000	...
p_1	1	1	1	2.2
p_2	2.5	2.6	2.4	3.4
p_3	6	4.2	7	...

Notes.
[a] A dominant component of the external radiation. IR: infrared dust emission, BEL: broad emission lines.
[b] Radius of source emission region.
[c] Magnetic field intensity at the distance of 1 pc.
[d] Energy density of the dominant component of the external radiation in the jet comoving frame at the given distance r.

observed at Period E ($\Gamma = 2.64 \pm 0.32$, see Table 1), the peak of the ERC-IR component in the Model E1 falls at ~800 MeV, in the *Fermi*-LAT band.

The far-IR spectral break in Period D requires a sharp break in the electron distribution function at $\gamma_{br1} = 800$. As the cooling break is expected at $\gamma_c \sim 3m_e c^2/(2\sigma_T R u'_{ext}) \sim 660$ (where R is a radius of source emission region and u'_{ext} is the energy density of the external radiation in the jet comoving frame), γ_{br1} is located just within the fast-cooling regime. The electron distribution in the fast-cooling regime cannot be harder than $p = 2$, hence the resulting synchrotron spectral index $\alpha = (p-1)/2$ should be larger than 0.5. In fact, the mean value of the observed spectral index between 70 μm and 160 μm is smaller than 0.5 ($\alpha_{70-160} = 0.35 \pm 0.23$), which cannot be explained if the electron cooling is efficient. However, the uncertainty of the measurement does not allow us to reject this scenario.

5.2. The Jet Precession Scenario: Two Synchrotron Components

Alternatively, if the jet precession can cause the observed γ-ray flare event with the polarization swing, the γ-ray/optical emission can be generated much closer to the central black hole, even within the broad-line region (see also in Paper I). Therefore, we also attempted to model Period D placing the emitting region at r_{BEL}. For $\Gamma_j = 15$, with model parameters fitted using the synchrotron and ERC components, the X-ray flux is overproduced by the SSC process. To alleviate this problem, we increased the jet Lorentz factor to $\Gamma_j = 20$. In Figure 18, we show Model D2 with parameters listed in Table 5. The magnetic field strength scaled to the distance of 1 pc is almost the same as the value in Model D1. Because of a smaller size of emission region and higher energy density of the locally produced synchrotron radiation, the synchrotron self-absorption is able to produce a spectral cutoff at a higher frequency of $\sim 3 \times 10^{12}$ Hz (~100 μm), consistent with the far-IR break. This interpretation has an advantage that it also could explain the observed hard spectral index between 70 μm and 160 μm, even smaller than 0.5, independently of details of the electron energy distribution.

The low-energy synchrotron component, dominating the mm/sub-mm band, must be produced in a much larger region, placing it far outside the broad-line region. In Figure 18, we present Model A2, fitted to the SED at Period A. We kept the Lorentz factor and the magnetic field consistent with Model D2, but we set the source at the distance ~4 pc, the same as in Model E1. This low-state model of Period A can reproduce both observed X-ray and γ-ray spectra by a single broken power-law electron distribution. The γ-ray spectral index is consistent with the IR/optical/UV spectral index. The synchrotron

self-absorption is effective at $\sim 10^{11}$ Hz and the spectral peak is located in the mm/sub-mm band.

Those results suggest the existence of two synchrotron components: one peaking in the mm/sub-mm band and the other peaking in the mid-IR band. The component with the peak in the mid-IR band is more variable, and can be produced at shorter distances, within the broad-line region, where the far-IR break can be explained by the synchrotron self-absorption.

6. CONCLUSIONS

This paper reports details of the multi-band campaigns on the well-known blazar 3C 279 during the first two years of the *Fermi* mission between 2008 and 2010. Some key results were already presented in Paper I. Most important of them was the coincidence of a dramatic γ-ray/optical flare with a change in the optical polarization, which we interpreted as the result of a compact emitting region: either propagating along a curved relativistic jet or located at a constant distance in a precessing jet. In addition, we reported on an "isolated" X-ray flare, an event without a clear counterpart in other bands, and taking place a few months after the γ-ray/optical flare. Here, we extended the observation epoch until 2010 August yielding the best coverage of time-resolved SEDs ever collected for 3C 279 from radio through high-energy γ-ray bands. Based on those data, we arrived at several new conclusions about the structure and emission models of the relativistic jet in the quasar.

1. In the high-energy γ-ray band measured by *Fermi*-LAT, the source exhibited two prominent flares reaching as high as $\sim 3 \times 10^{-6}$ photons cm^{-2} s^{-1} above 100 MeV in the first year while it was in a relatively quiescent state in the second year. No significant correlation between flux and photon index has been measured in similarity to other LAT blazars. The two year averaged γ-ray spectral shape above 200 MeV clearly deviates from a single power law. The broken power-law model returns a break energy within a few GeV range, which does not appear to vary with the source flux. Such behavior is similar to that observed in other bright FSRQs.
2. The superb temporal coverage allowed us to measure in detail the cross-correlation of the γ-ray and optical fluxes. The optical signals appear to be delayed with respect to the γ-ray signals by $\sim$10 days. Such a lag can be explained in terms of the simple synchrotron and inverse-Compton model, in the scenario where a cloud containing ultra-relativistic electrons propagates down the jet through the regions where the ratio of the external radiation energy to the magnetic energy densities decrease with distance. We have verified this idea qualitatively (see the Appendix), but it still needs specific numerical modeling to be confirmed quantitatively.
3. X-ray observations reveal a pair of pronounced flares separated by $\sim$90 days. Those are not contemporaneous with a pair of bright γ-ray/optical flares—also separated by $\sim$90 days—but instead, are delayed with respect to the γ-ray/optical flares by about 155 days. Because of such a long delay, it seems implausible that these events are causally related. Instead, the possible scenarios of the X-ray flares may involve changes of the source parameters such as the jet direction, Lorentz factor, and/or location of the dissipation event, or may require more "exotic" solutions, for instance, bulk-Compton process, inefficient electron acceleration above a given energy, and hadronic processes. At this stage we cannot discriminate among any of those scenarios.
4. The spectral coverage of the infrared band with *Spitzer* enabled us to probe the detailed structure of the low-energy spectral bump, attributed to the synchrotron radiation. Significant spectral variability, with soft/power-law spectra in the low state and hard/curved spectra in the high state, as well as the detection of a sharp far-IR spectral break in the high state, strongly suggest the existence of two synchrotron components: one peaking in the mm/sub-mm band and the other peaking in the mid-IR band. The component with a peak at the mid-IR band can be responsible for emission during γ-ray flaring states.
5. We have applied our leptonic emission model for the SEDs during the γ-ray flaring state with a polarization change. Adopting the interpretation of the polarization swing involving the propagation of the emitting region—that suggested in Paper I—we can explain the evolution of the broadband SEDs from Periods D to E during the γ-ray flaring event by a shift of the position of the emitting region and a change of the viewing angle that are consistent with its trajectory. We used the same distribution of magnetic fields and only slightly changed electron spectra, but required a rather steep stratification of the external radiation density in the form of thermal emission from the dusty torus. In this case, the far-IR spectral break requires a break in the electron distribution. The observed *Spitzer*-MIPS spectral index $\alpha_{70-160} = 0.35 \pm 0.23$ is marginally consistent with the synchrotron emission in the fast-cooling regime.
6. We also discussed the model in which the γ-ray flare is generated within the broad emission line region at sub-pc scale from the central black hole according to the jet precession scenario. This model explains the mid-IR break during the flaring state of Period D by synchrotron self-absorption. Here, we also discussed the low-state SED in Period A where the mm/sub-mm band peaking synchrotron component can be dominant. The model shows the related ERC component can explain the steady X-ray emission.

The *Fermi*-LAT Collaboration acknowledges generous ongoing support from a number of agencies and institutes that have supported both the development and the operation of the LAT as well as scientific data analysis. These include the National Aeronautics and Space Administration and the Department of Energy in the United States, the Commissariat à l'Energie Atomique and the Centre National de la Recherche Scientifique/Institut National de Physique Nucléaire et de Physique des Particules in France, the Agenzia Spaziale Italiana and the Istituto Nazionale di Fisica Nucleare in Italy, the Ministry of Education, Culture, Sports, Science and Technology (MEXT), High Energy Accelerator Research Organization (KEK), and Japan Aerospace Exploration Agency (JAXA) in Japan, and the K. A. Wallenberg Foundation, the Swedish Research Council, and the Swedish National Space Board in Sweden. Additional support for science analysis during the operations phase is gratefully acknowledged from the Istituto Nazionale di Astrofisica in Italy and the Centre National d'Études Spatiales in France.

The Submillimeter Array is a joint project between the Smithsonian Astrophysical Observatory and the Academia Sinica Institute of Astronomy and Astrophysics and is funded by the Smithsonian Institution and the Academia Sinica. The St. Petersburg University team acknowledges support from the

Russian RFBR foundation via grant 09-02-00092. AZT-24 observations are made within an agreement between Pulkovo, Rome, and Teramo observatories. This paper is partly based on observations carried out at the German-Spanish Calar Alto Observatory, which is jointly operated by the MPIA and the IAA-CSIC. Acquisition of the MAPCAT data is supported in part by MICIIN (Spain) grant and AYA2010-14844, and by CEIC (Andalucía) grant P09-FQM-4784. The Metsähovi team acknowledges the support from the Academy of Finland to our observing projects (numbers 212656, 210338, 121148, and others). The Medicina and Noto telescopes are operated by INAF-Istituto di Radioastronomia. The research at Boston University was supported by NASA Fermi GI grants NNX08AV65G, NNX08AV61G, NNX09AT99G, and NNX09AU10G, and NSF grant AST-0907893. The PRISM camera at Lowell Observatory was developed by K. Janes et al. at BU and Lowell Observatory, with funding from the NSF, BU, and Lowell Observatory. The Liverpool Telescope is operated on the island of La Palma by Liverpool John Moores University in the Spanish Observatorio del Roque de los Muchachos of the Instituto de Astrofisica de Canarias, with funding from the UK Science and Technology Facilities Council. The Abastumani Observatory team acknowledges financial support by the Georgian National Science Foundation through grant GNSF/ST09/521 4-320. The research at the University of Michigan has been funded by a series of grants from NASA and from the NSF. Specific grant numbers are NASA grants NNX09AU16G, NNX10AP16G, NNX11AO13G, and NSF grant AST-0607523. Funding for the operation of UMRAO was provided by the University of Michigan.

M.H. is supported by the Research Fellowships of the Japan Society for the Promotion of Science for Young Scientists. This work was partially supported by the Polish MNiSW grants N N203 301635 and N N203 386337, the Polish ASTRONET grant 621/E-78/SN-0068/2007, and the Polish NCN grant DEC-2011/01/B/ST9/04845.

APPENDIX

POSSIBLE EXPLANATION OF A LAG BETWEEN THE γ-RAY AND OPTICAL FLARES

As we discussed in Section 4.1, the multi-band time series imply that during the flaring activity detected in 3C 279 the optical emission appears to be delayed with respect to the γ-ray emission. In the context of radiation models adopted here (Section 5), the same electron population produces optical synchrotron photons and also inverse-Compton γ-rays *in the fast-cooling regime*. A lag between the optical and γ-ray flares may therefore result from different profiles of decrease of the magnetic energy density $u'_{\rm B}(r)$ and the external (target) radiation energy density $u'_{\rm ext}(r)$ with the distance r along the jet, convolved with a non-monotonic profile of the electron injection rate within the outflow.

In the fast-cooling (FC) regime, the power injected into the relativistic particles $P_{\rm e,\,inj}$ is immediately radiated away and determines the total broadband luminosity produced by the cooled electrons $L_{\rm tot,\,FC}$. Assuming a strong inverse-Compton dominance, i.e., the observed inverse-Compton peak (γ-ray) luminosity $\simeq L_\gamma$ being much larger than the observed synchrotron peak (optical) luminosity $L_{\rm opt}$, one has

$$P_{\rm e,\,inj}(r) \propto L_{\rm tot,\,FC}(r) \simeq L_\gamma(r) + L_{\rm opt}(r) \sim L_\gamma(r), \qquad \text{(A1)}$$

while the optical luminosity is

$$L_{\rm opt}(r) \simeq \frac{u'_{\rm B}(r)}{u'_{\rm ext}(r)}\, L_\gamma(r) \propto \frac{u'_{\rm B}(r)}{u'_{\rm ext}(r)}\, P_{\rm e,\,inj}(r), \qquad \text{(A2)}$$

where we assumed $\delta = \Gamma_{\rm j}$ being independent on the position r along the jet. Hence, it is clear that while a maximum of $L_\gamma(r)$ is determined solely by the injection rate $P_{\rm e,\,inj}(r)$, a maximum of $L_{\rm opt}(r)$ may in general be quite different, depending on particular radial profiles of $P_{\rm e,\,inj}(r)$ and of the ratio $[u'_{\rm B}/u'_{\rm ext}]$ (r).

As a specific illustrative example, let us assume that the dissipation region propagating down the jet injects non-thermal energy into radiating particles at the rate being a broad Gaussian function of distance r with a maximum at r_0 and a width of $r_0/\sqrt{2}$,

$$P_{\rm e,\,inj} \propto \exp\big[-(r-r_0)^2/r_0^2\big], \qquad \text{(A3)}$$

and that magnetic field and external photon field energy densities scale with r as power laws with indices $\beta_{\rm B}$ and $\beta_{\rm ext}$,

$$u'_{\rm B}(r) \propto r^{-\beta_{\rm B}} \quad \text{and} \quad u'_{\rm ext}(r) \propto r^{-\beta_{\rm ext}}. \qquad \text{(A4)}$$

Then one can find that L_γ has a maximum at $r = r_0$, as expected, whereas $L_{\rm opt}$ attains a maximum at

$$r_{\rm cr} = \frac{r_0}{2} \times \left(1 + \sqrt{1 + 2\,(\beta_{\rm ext} - \beta_B)}\right), \qquad \text{(A5)}$$

which is larger than r_0 as long as $\beta_{\rm ext} > \beta_{\rm B}$ and thus results in the optical flare lagging the γ-ray flare. This is due to the fact that with the magnetic energy density decreasing less rapidly in the jet comoving frame than the external radiation energy density, the drop in the injection rate $P_{\rm e,\,inj}(r)$ between r_0 and $r_{\rm cr}$ is compensated by the *increase* in the ratio $[u'_{\rm B}/u'_{\rm ext}]$ (r).

Let us further consider the particular values of $\beta_{\rm B} = 2$ and $\beta_{\rm ext} = 4$ discussed in Section 5. With such, assuming again the electron injection rate being a broad Gaussian function of the distance r along the jet as in the example above, the observed time lag between the optical and γ-ray flares $\Delta t_{\rm obs}$ can be evaluated as roughly

$$\Delta t_{\rm obs} \simeq \frac{0.6\, r_0}{c\, \Gamma_{\rm j}^2} \simeq 3 \times \left(\frac{\Gamma_{\rm j}}{15}\right)^{-2} \left(\frac{r_0}{1\,{\rm pc}}\right) \text{ days}. \qquad \text{(A6)}$$

It is encouraging that a 10 day lag is expected for $\Gamma_{\rm j} \simeq 15$ and $r_0 \simeq 3$ pc, which are the bulk Lorentz factor and the location of the dissipation region comparable to that inferred from our ERC-IR modeling.

REFERENCES

Abazajian, K. N., Adelman-McCarthy, J. K., Agüeros, M. A., et al. 2009, ApJS, 182, 543
Abdo, A. A., Ackermann, M., Agudo, I., et al. (*Fermi*-LAT Collaboration) 2010a, ApJ, 721, 1425
Abdo, A. A., Ackermann, M., Ajello, M., et al. (*Fermi*-LAT Collaboration) 2009a, Astropart. Phys., 32, 193
Abdo, A. A., Ackermann, M., Ajello, M., et al. (*Fermi*-LAT Collaboration) 2009b, ApJ, 699, 817
Abdo, A. A., Ackermann, M., Ajello, M., et al. (*Fermi*-LAT Collaboration) 2010b, Nature, 463, 919
Abdo, A. A., Ackermann, M., Ajello, M., et al. (*Fermi*-LAT Collaboration) 2010c, ApJS, 188, 405
Abdo, A. A., Ackermann, M., Ajello, M., et al. (*Fermi*-LAT Collaboration) 2010d, ApJ, 710, 810
Abdo, A. A., Ackermann, M., Ajello, M., et al. (*Fermi*-LAT Collaboration) 2010e, ApJ, 710, 1271

Abdo, A. A., Ackermann, M., Ajello, M., et al. (*Fermi*-LAT Collaboration) 2010f, ApJ, 722, 520
Abdo, A. A., Ackermann, M., Ajello, M., et al. (*Fermi*-LAT Collaboration) 2010g, Phys. Rev. Lett., 104, 101101
Abdo, A. A., Ackermann, M., Ajello, M., et al. (*Fermi*-LAT Collaboration) 2011, ApJ, 726, 43
Ackermann, M., Ajello, M., Baldini, L., et al. (*Fermi*-LAT Collaboration) 2010, ApJ, 721, 1383
Ackermann, M., Ajello, M., Ballet, J., et al. (*Fermi*-LAT Collaboration) 2012, ApJ, 751, 159
Agudo, I., Jorstad, S. G., Marscher, A. P., et al. 2011a, ApJ, 726, L13
Agudo, I., Marscher, A. P., Jorstad, S. G., et al. 2011b, ApJ, 735, L10
Albert, J., Aliu, E., Anderhub, H., et al. (MAGIC Collaboration) 2008, Science, 320, 1752
Aleksić, J., Antonelli, L. A., Antoranz, P., et al. (MAGIC Collaboration) 2011, A&A, 530, A4
Atwood, W. B., Abdo, A. A., Ackermann, M., et al. (*Fermi*-LAT Collaboration) 2009, ApJ, 697, 1071
Baars, J. W. M., Genzel, R., Pauliny-Toth, I. I. K., & Witzel, A. 1977, A&A, 61, 99
Begelman, M. C., & Sikora, M. 1987, ApJ, 322, 650
Bessell, M. S., Castelli, F., & Plez, B. 1998, A&A, 333, 231
Blandford, R. D., & Levinson, A. 1995, ApJ, 441, 79
Bloom, S. D., & Marscher, A. P. 1996, ApJ, 461, 657
Bock, D. C.-J., Bolatto, A. D., Hawkins, D. W., et al. 2006, Proc. SPIE, 6267, 13
Bonning, E. W., Bailyn, C., Urry, C. M., et al. 2009, ApJ, 697, L81
Cardelli, J. A., Clayton, G. C., & Mathis, J. S. 1989, ApJ, 345, 245
Chatterjee, R., Jorstad, S. G., Marscher, A. P., et al. 2008, ApJ, 689, 79
Collmar, W., Böttcher, M., Krichbaum, T. P., et al. 2010, A&A, 522, A66
Collmar, W., Schönfelder, V., Zhang, S., et al. 2001, in AIP Conf. Proc. 587, Gamma 2001: Gamma-Ray Astrophysics, ed. S. Ritz, N. Gehrels, & C. R. Shroder (Melville, NY: AIP), 271
Cutri, R. M., Skrutskie, M. F., van Dyk, S., et al. 2003, VizieR Online Data Catalog, 2246, 0
Daly, R. A., & Marscher, A. P. 1988, ApJ, 334, 539
D'Ammando, F., Raiteri, C. M., Villata, M., et al. 2011, A&A, 529, A145
Dermer, C. D., & Schlickeiser, R. 1993, ApJ, 416, 458
Dermer, C. D., Schlickeiser, R., & Mastichiadis, A. 1992, A&A, 256, L27
Eachus, L. J., & Liller, W. 1975, ApJ, 200, L61
Edelson, R., Turner, T. J., Pounds, K., et al. 2002, ApJ, 568, 610
Edelson, R. A., & Krolik, J. H. 1988, ApJ, 333, 646
Engelbracht, C. W., Blaylock, M., Su, K. Y. L., et al. 2007, PASP, 119, 994
Giuliani, A., D'Ammando, F., Vercellone, S., et al. 2009, A&A, 494, 509
Gordon, C. W., Engelbracht, C. W., Fadda, D., et al. 2007, PASP, 119, 1019
Greiner, J., Bornemann, W., Clemens, C., et al. 2008, PASP, 120, 405
Gu, M., Cao, X., & Jiang, D. R. 2001, MNRAS, 327, 1111
Hartman, R. C., Bertsch, D. L., Bloom, S. D., et al. 1999, ApJS, 123, 79
Hartman, R. C., Bertsch, D. L., Fichtel, C. E., et al. 1992, ApJ, 385, L1
Hartman, R. C., Böttcher, M., Aldering, G., et al. 2001a, ApJ, 553, 683
Hartman, R. C., Villata, M., Balonek, T. J., et al. 2001b, ApJ, 558, 583
Hermsen, W., Aarts, H. J. M., Bennett, K., et al. 1993, A&AS, 97, 97
Homan, D. C., Lister, M. L., Kellermann, K. I., et al. 2003, ApJ, 589, L9
Jorstad, S. G., Marscher, A. P., Larionov, V. M., et al. 2010, ApJ, 715, 362
Jorstad, S. G., Marscher, A. P., Lister, M. L., et al. 2004, AJ, 127, 3115
Jorstad, S. G., Marscher, A. P., Lister, M. L., et al. 2005, AJ, 130, 1418
Kalberla, P. M. W., Burton, W. B., Hartmann, D., et al. 2005, A&A, 440, 775
Komissarov, S. S., & Falle, S. A. E. G. 1997, MNRAS, 288, 833
Koyama, K., Tsunemi, H., Dotani, T., et al. 2007, PASJ, 59, 23
Krühler, T., Küpcü Yoldaş, A., Greiner, J., et al. 2008, ApJ, 685, 376
Larionov, V. M., Jorstad, S. G., Marscher, A. P., et al. 2008, A&A, 492, 389
Lynds, C. R., Stockton, A. N., & Livingston, W. C. 1965, ApJ, 142, 1667
Mannheim, K., & Biermann, P. L. 1992, A&A, 253, L21
Maraschi, L., Ghisellini, G., & Celotti, A. 1992, ApJ, 397, L5
Maraschi, L., Grandi, P., Urry, C. M., et al. 1994, ApJ, 435, L91
Mattox, J. R., Bertsch, D. L., Chiang, J., et al. 1996, ApJ, 461, 396
McNaron-Brown, K., Johnson, W. N., Jung, G. V., et al. 1995, ApJ, 451, 575
Mitsuda, K., Bautz, M., Inoue, H., et al. 2007, PASJ, 59, 1
Moderski, R., Sikora, M., & Błażejowski, M. 2003, A&A, 406, 855
Mor, R., & Netzer, H. 2012, MNRAS, 420, 526
Morrison, R., & McCammon, D. 1983, ApJ, 270, 119
Nalewajko, K. 2010, Int. J. Mod. Phys. D, 19, 701
Nalewajko, K., & Sikora, M. 2009, MNRAS, 392, 1205
Nandikotkur, G., Jahoda, K. M., Hartman, R. C., et al. 2007, ApJ, 657, 706
Nandra, K., George, I. M., Mushotzky, R. F., Turner, T. J., & Yaqoob, T. 1997, ApJ, 476, 70
Nilsson, K., Pursimo, T., Villforth, C., Lindfors, E., & Takalo, L. O. 2009, A&A, 505, 601
Ogle, P. M., Wehrle, A. E., Balonek, T., & Gurwell, M. A. 2011, ApJS, 195, 19
Pian, E., Urry, C. M., Maraschi, L., et al. 1999, ApJ, 521, 112
Poole, T. S., Breeveld, A. A., Page, M. J., et al. 2008, MNRAS, 383, 627
Poutanen, J., & Stern, B. 2010, ApJ, 717, L118
Raiteri, C. M., Villata, M., Aller, M. F., et al. 2011, A&A, 534, A87
Raiteri, C. M., Villata, M., Lanteri, L., Cavallone, M., & Sobrito, G. 1998, A&AS, 130, 495
Reach, W. T., Megeath, S. T., Cohen, M., et al. 2005, PASP, 117, 978
Richards, J. L., Max-Moerbeck, W., Pavlidou, V., et al. 2011, ApJS, 194, 29
Roming, P. W. A., Kennedy, T. E., Mason, K. O., et al. 2005, Space Sci. Rev., 120, 95
Sault, R. J., Teuben, P. J., & Wright, M. C. H. 1995, in ASP Conf. Ser. 77, Astronomical Data Analysis Software and Systems IV, ed. R. A. Shaw, H. E. Payne, & J. J. E. Hayes (San Francisco, CA: ASP), 433
Schlegel, D. J., Finkbeiner, D. P., & Davis, M. 1998, ApJ, 500, 525
Sikora, M. 2011, in IAU Symp. 275, Jets at All Scales, ed. G. E. Romero, R. A. Sunyaev, & T. Belloni (Cambridge: Cambridge Univ. Press), 59
Sikora, M., Begelman, M. C., & Rees, M. J. 1994, ApJ, 421, 153
Sikora, M., Stawarz, Ł., Moderski, R., Nalewajko, K., & Madejski, G. M. 2009, ApJ, 704, 38
Skrutskie, M. F., Cutri, R. M., Stiening, R., et al. 2006, AJ, 131, 1163
Stansberry, J. A., Gordon, K. D., Bhattacharya, B., et al. 2007, PASP, 119, 1038
Takahashi, T., Abe, K., Endo, M., et al. 2007, PASJ, 59, 35
Tanaka, Y. T., Stawarz, Ł., Thompson, D. J., et al. 2011, ApJ, 733, 19
Tody, D. 1993, in ASP Conf. Ser. 52, Astronomical Data Analysis Software and Systems II, ed. R. J. Hanisch, R. J. V. Brissenden, & J. Barnes (San Francisco, CA: ASP), 173
Ulrich, M.-H., Maraschi, L., & Urry, C. M. 1997, ARA&A, 35, 445
Vaughan, S., Edelson, R., Warwick, R. S., & Uttley, P. 2003, MNRAS, 345, 1271
Villata, M., Raiteri, C. M., Ghisellini, G., et al. 1997, A&AS, 121, 119
Villata, M., Raiteri, C. M., Gurwell, M. A., et al. 2009, A&A, 504, L9
Villata, M., Raiteri, C. M., Larionov, V. M., et al. 2008, A&A, 481, L79
Watanabe, M., Nakaya, H., Yamamuro, T., et al. 2005, PASP, 117, 870
Wehrle, A. E., Pian, E., Urry, C. M., et al. 1998, ApJ, 497, 178
Wolff, M. J., Nordsieck, K. H., & Nook, M. A. 1996, AJ, 111, 856
Woo, J.-H., & Urry, C. M. 2002, ApJ, 579, 530